

Ro-vibrational excitation of an organic molecule (HCN) in protoplanetary disks

Simon Bruderer¹, Daniel Harsono^{2,3}, and Ewine F. van Dishoeck^{2,1}

¹ Max-Planck-Institut für Extraterrestrische Physik, Gießenbachstrasse 1, 85748 Garching, Germany

² Leiden Observatory, Leiden University, P.O. Box 9513, 2300 RA Leiden, The Netherlands

³ SRON Netherlands Institute for Space Research, PO Box 800, 9700 AV, Groningen, The Netherlands

Accepted version – July 26, 2018

ABSTRACT

Context. Organic molecules are important constituents of protoplanetary disks. Their ro-vibrational lines observed in the near- and mid-infrared are commonly detected toward T Tauri disks. These lines are the only way to probe the chemistry in the inner few au where terrestrial planets form. To understand this chemistry, accurate molecular abundances have to be determined. This is complicated by excitation effects that include radiative pumping. Most analyses so far have made the assumption of local thermal equilibrium (LTE), which may not be fulfilled because of the high gas densities required to collisionally thermalize the vibrational levels of the molecules.

Aims. The non-LTE excitation effects of hydrogen cyanide (HCN) are studied to evaluate (i) how the abundance determination is affected by the LTE assumption, (ii) whether the ro-vibrational excitation is dominated by collisions or radiative pumping, and (iii) which regions of protoplanetary disks are traced by certain vibrational bands.

Methods. Starting from estimates for the collisional rate coefficients of HCN, non-LTE slab models of the HCN emission were calculated to study the importance of different excitation mechanisms. Using a new radiative transfer model, the HCN emission from a full two-dimensional disk was then modeled to study the effect of the non-LTE excitation, together with the line formation. We ran models tailored to the T Tauri disk AS 205 (N) where HCN lines in both the 3 μm and 14 μm bands have been observed by VLT-CRIRES and the *Spitzer Space Telescope*.

Results. Reproducing the observed 3 μm / 14 μm flux ratios requires very high densities and kinetic temperatures ($n > 10^{14} \text{ cm}^{-3}$ and $T > 750 \text{ K}$), if only collisional excitation is accounted for. Radiative pumping can, however, excite the lines easily out to considerable radii $\sim 10 \text{ au}$. Consequently, abundances derived from LTE and non-LTE models do not differ by more than a factor of about 3. Models with both a strongly enhanced abundance within $\sim 1 \text{ au}$ (jump abundance) and constant abundance can reproduce the current observations, but future observations with the MIRI instrument on JWST and METIS on the E-ELT can easily distinguish between the scenarios and test chemical models. Depending on the scenario, ALMA can detect rotational lines within vibrationally excited levels.

Conclusions. Pumping by the continuum radiation field can bring HCN close enough to the LTE so that no big deviations in derived abundances are introduced with the LTE assumption, but the line profiles are substantially altered. In non-LTE models, accounting for collisional and radiative excitation, the emitting region can be much larger than in LTE models. Because HCN can be radiatively pumped to considerable radii, deriving a small emitting region from observations can thus point to the chemical abundance structure (e.g., jump abundance). Owing to their level structure, CO_2 and C_2H_2 are expected to act in a similar way, facilitating studies of the warm inner disk chemistry.

Key words. Protoplanetary disks – Molecular processes – Astrochemistry – Radiative transfer – Line: formation

1. Introduction

Organic molecules play an important role in the chemistry of planet-forming zones. These molecules are the initial step toward forming the prebiotic molecules that ultimately lead to life. They are also important tracers of the physical and chemical conditions in protoplanetary disks (Bergin et al. 2007; Herbst & van Dishoeck 2009; Pontoppidan et al. 2014 for reviews). A surprising finding of the *Spitzer Space Telescope* was the rich mid-infrared (mid-IR) spectrum from the innermost few au containing organic molecules (Lahuis et al. 2006; Salyk et al. 2008; Carr & Najita 2008). Different disk radii can be probed by combining submillimeter to near-IR wavelengths, since these lines span a wide range of level energies. New facilities such

as the *Atacama Large Millimeter/submillimeter Array* (ALMA), the *Very Large Telescope* (VLT), or the future *James Webb Space Telescope* (JWST) and *E-European Extremely Large Telescope* (E-ELT), pave the way for such multiwavelength observations at high spatial resolution and good sensitivity. To make progress in understanding the chemical structure of protoplanetary disks and the chemical history of planetary atmospheres and comets, accurate abundances have to be derived. This is complicated by excitation and radiative transfer effects. In this work, we study the non-LTE vibrational excitation and radiative transfer effects of HCN.

Hydrogen cyanide (HCN) is a simple organic molecule, but an important reactant for producing more complex nitrogen-bearing molecules, building blocks of amino acids such as adenine (Agúndez et al. 2008; Walsh et al. 2014; Bast et al. 2013). Together with acetylene (C_2H_2) and methane (CH_4), HCN is one of the bottlenecks in producing more complex species. Owing

Send offprint requests to: Simon Bruderer,
e-mail: simonbruderer@gmail.com

to the high activation energies of the formation reactions, these molecules are strongly enhanced in the innermost 1 au of a typical T Tauri disk (Agúndez et al. 2008; Bast et al. 2013). For example, $\text{CN} + \text{H}_2 + \Delta E \rightarrow \text{HCN} + \text{H}$ has an activation barrier of $\Delta E = 820$ K. Because of the enhanced HCN abundance in the innermost region of protoplanetary disks, this molecule may be one of the best tracers of the conditions in terrestrial planet-forming regions.

Trends of HCN emission relative to other molecules have been found observationally. An increase in the mid-IR HCN/H₂O ratio with disk mass measured by the submillimeter continuum is found by Najita et al. (2013) (see also Najita et al. 2011) and explained by a larger number of non-migrating planetesimals in more massive disks locking up water ice beyond the snow line. However, toward very low mass stars, this trend does not hold (Pascucci et al. 2013). The HCN/C₂H₂ mid-IR emission ratio was found to be significantly higher around Sun-like stars compared to brown dwarfs which was interpreted by a different physical and chemical evolution of the protoplanetary disks (Pascucci et al. 2009). So far, these trends have only been discussed in the context of simple LTE slab models. However, to answer the question if trends are the consequence of excitation or abundance structure, a more complete modeling accounting for non-LTE excitation effects needs to be carried out.

HCN has a dipole moment and can be observed through pure rotational lines at submillimeter wavelengths and ro-vibrational transitions in the infrared. Besides CO and H₂O, HCN is currently one of the few molecules with such multiwavelength detections towards protoplanetary disks. It is detected at submillimeter wavelengths (Dutrey et al. 1997; Kastner et al. 1997; van Zadelhoff et al. 2001; Thi et al. 2004; Öberg et al. 2010, 2011; Chapillon et al. 2012), in the mid-IR (Carr & Najita 2008; Pontoppidan et al. 2010; Salyk et al. 2011), and in the near-IR (Gibb et al. 2007; Doppmann et al. 2008; Mandell et al. 2012). Towards massive young stellar objects rotational lines of HCN within vibrationally excited levels have also been observed (e.g., Boonman et al. 2001; Benz et al. 2007; Veach et al. 2013). Vibrational lines¹ from the ν_2 bending mode at 14 μm have been observed spectrally unresolved by *Spitzer* (Lahuis et al. 2006). The ν_1 H-C stretching mode at 3 μm is observed with the VLT *CRyogenic high-resolution InfraRed Echelle Spectrograph* (CRIRES) and NIRSPEC on Keck. In the near future, the VLT *Imager and Spectrometer for mid Infrared II* (VISIR-II) and the *Texas Echelon Cross Echelle Spectrograph* (TEXES) on Gemini North will be able to spectrally resolve the 14 μm lines. With the *Mid-Infrared Instrument* (MIRI) and the *Near-Infrared Spectrograph* (NIRSpec) on the JWST and the *Mid-infrared E-ELT Imager and Spectrograph* (METIS), it will be possible to study the entire 3 – 14 μm wavelength range at much higher sensitivity and spectral resolution also allowing observation of the $2\nu_2 - \nu_2$ mode at 7 μm .

The analysis of HCN vibrational lines has so far mostly relied on the LTE assumption. This means that the HCN level population is driven to thermalization, usually assumed to be by collisions with the main constituent of the molecular gas, H₂. However, the so-called *critical density* n_{crit} , needed to provide enough collisions for thermalization, is for vibrational transitions orders of magnitude larger than for pure rotational lines ($n_{\text{crit}} \sim 10^8 \text{ cm}^{-3}$ for HCN $J = 4 - 3$). Towards massive protostars, Boonman et al. (2003) thus estimate based on a simple

model, that HCN is more likely pumped by infrared continuum radiation of the warm dust than collisionally excited. This is similar to the vibrational bands HCN in comets which are pumped radiatively by solar radiation (e.g., Paganini et al. 2010). In protoplanetary disks, the critical densities of vibrational transitions can be reached. However, the dust optical depths towards such dense regions is likely large and shields the molecular emission. A comprehensive model of the HCN emission from protoplanetary disks should thus account for radiative pumping and collisional excitation effects as well as the line formation process like shielding of line emission by dust. So far, only a few studies on the vibrational excitation of molecules in protoplanetary disks have been carried out, like Meijerink et al. (2009) on water and Blake & Boogert (2004); Thi et al. (2013) on CO.

In this work, the non-LTE emission of HCN from protoplanetary disks is modeled. We derive an approximate set of vibrational collision rate coefficients, based on measured values and calculate the non-LTE emission from a simple slab to study the relative importance of different processes. We next model the HCN emission of the protoplanetary disk AS 205 (N), where both the 14 μm band has been observed by *Spitzer* (Salyk et al. 2011) and the 3 μm lines by VLT-CRIRES (Mandell et al. 2012). While this work concentrates on this particular disk as an example, a parameter study is carried out to find the general trends. The main questions to be answered by our work are: How much does the abundance determination change if non-LTE effects are included? How are different vibrational bands of HCN excited (radiative or collisional excitation)? What do different HCN lines tell about the radial and vertical abundance structure?

The paper is organized as follows: In Sect. 2 the molecular structure is summarized and slab models run to study the relative importance of collisional and radiative excitation. Sect. 3 presents non-LTE models of a protoplanetary disk and a study of the dependence of the emission on various parameters like the HCN abundance structure, the gas-to-dust ratio or the dust opacity. The results are discussed in Sect. 4 followed by a conclusions section (Sect. 5).

2. The ro-vibrational excitation of HCN

To study the relative importance of different excitation mechanisms independent of geometry, we first discuss simple slab models at constant physical conditions (density, kinetic temperature and continuum radiation field). The steady state level population is then given by the rate equations (e.g., van der Tak et al. 2007),

$$\frac{dn_i}{dt} = \sum_{i \neq j} n_j P_{ji} - n_i \sum_{i \neq j} P_{ij} = 0, \quad (1)$$

where n_i (cm^{-3}) is the population of a level designated with an index i and P_{ij} (s^{-1}) is the rate coefficient for the transition between levels i and j . The rates of different collisional and radiative processes enter through

$$P_{ij} = \begin{cases} A_{ij} + B_{ij}\langle J_{ij} \rangle + K_{ij}n & (E_i > E_j) \\ B_{ij}\langle J_{ij} \rangle + K_{ij}n & (E_i < E_j), \end{cases} \quad (2)$$

with the Einstein- A_{ij} and B_{ij} coefficients for spontaneous and induced emission between levels i and j , the local radiation field $\langle J_{ij} \rangle$ averaged over angles and local line profile function, the collisional rate coefficient K_{ij} , and the collisional partner density n . Spontaneous decay from level i to level j is only possible if the level energy $E_j < E_i$. The level population controls the emission

¹ Note that different definitions of the vibrational modes are used. Here, ν_1 refers to the H-C stretching mode, ν_2 to the bending mode, and ν_3 to the C-N stretching mode, following the definition by the NIST.

of line photons and the line opacity. Thus, through the radiation field $\langle J_{ij} \rangle$ the level population enters Eq. 1 complicating the problem considerably. Once a self-consistent solution of level population and radiation field is found, the emitted emission is obtained from the solution of the radiative transfer equation.

The slab models presented in this section are calculated using the RADEX code (van der Tak et al. 2007). This code approximates the contribution of the line photons to the radiation field by an analytical function of the level population, using the so-called escape probability formalism (e.g., Sobolev 1960). Initial exploration with a limited model was performed by Bast (2013).

2.1. A model molecule for HCN

For the excitation calculation a model molecule of HCN needs to be constructed. The same 7 vibrational levels are included as González-Alfonso & Cernicharo (1999) and Cernicharo et al. (1999) used to model the vibrational emission of radiatively pumped HCN towards AGB stars. Figure 1 shows the included energy levels and vibrational band wavelengths. We include l -type splitting of the levels in the ν_2 bending mode with simultaneous rotation along the internuclear axis ($l > 0$). Including 3 levels with l -type splitting, there is thus a total number of 10 vibrational levels, each with 60 rotational levels. The effect of other vibrational levels is not expected to become important, as they are not radiatively connected to the ground state (González-Alfonso & Cernicharo 1999). In particular, the ν_3 modes have very low Einstein-A coefficients and are not included. Hyperfine splitting is not included, as our observations do not spectrally resolve individual hyperfine components. The electronic structure of HCN is quite complicated, due to intramolecular isomerization HCN - HNC above ~ 2.1 eV (e.g., Barger et al. 2003) but this does not affect the levels considered here. The photoabsorption bands in the UV are all dissociative (Lee 1984) and we thus do not account for UV pumping or fluorescence. Chemical pumping has been suggested to explain a submillimeter maser within the 04^0_0 band observed towards IRC +10216, but is unlikely to affect lower lying vibrational bands (Schilke et al. 2000).

The level energies and radiative transition probabilities (Einstein-A coefficients) are taken from Barber et al. (2014). To model H^{13}CN , energies and transition probabilities by Harris et al. (2008) are used. A total of 602 levels and 4622 radiative transitions are included. No collisional rate coefficients for the vibrational levels of HCN are available. As for CO or water approximations are needed here (Faure & Josselin 2008; Thi et al. 2013). Based on measured H_2 - HCN collisional rate coefficients for the total $110 \rightarrow 000$ and $100 \rightarrow 000$ bands (Smith & Warr 1991), a full set of collisional rate coefficients is constructed by combining these measured vibrational rates with pure rotational collision rates by Dumouchel et al. (2010). Our procedure follows the approach of Faure & Josselin (2008) and Thi et al. (2013) and is described in detail in Appendix B. The main assumption is that vibrational and rotational collisional rates can be decoupled. An assessment of the collisional rate uncertainty is difficult, but they are probably within an order of magnitude as estimated for the water rates by Faure & Josselin (2008). We only account for H_2 -HCN collisions, as the critical densities of vibrational transitions are very high ($> 10^{10} \text{ cm}^{-3}$) and gas is purely molecular in protoplanetary disks even at much lower densities.

To test the completeness of our model molecule, we have calculated the AS 205 (N) models presented in Table 2 also

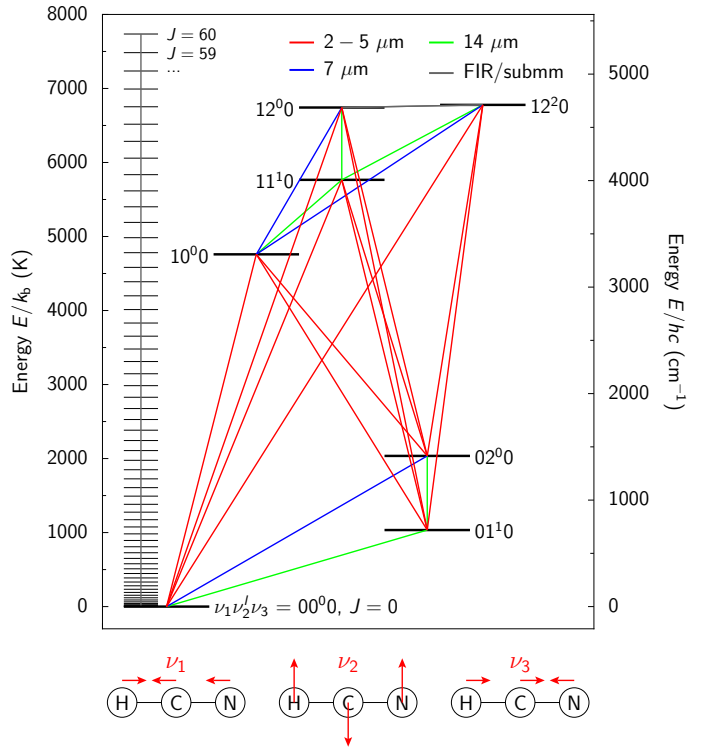


Fig. 1. HCN level structure considered in this work. Red lines denote vibrational bands at wavelengths of 2 – 5 μm , while blue and green lines indicate bands at 7 μm and 14 μm , respectively. The vibrational modes ν_1 , ν_2 , and ν_3 are shown below the level diagram. For clarity, the rotational ladder is only shown for the vibrational ground state.

with a reduced model molecule including only the vibrational ground state and the ν_1 and ν_2 modes. This reduced model molecule yields fluxes within 20 % compared to the larger model molecule. The small deviation is understood by the fact that most of the molecules remain in the vibrational ground state throughout the disk and radiative pumping through a vibrational band is followed by decay through the same band.

2.2. The HCN spectrum

A full spectrum of HCN from 2 μm to the pure rotational submillimeter lines from a slab model is shown in Figure 2. We chose a kinetic temperature of 750 K and a column density of $2 \times 10^{15} \text{ cm}^{-2}$, in agreement with typical values found by Salyk et al. (2011). A Gaussian line profile with a FWHM line width of $\Delta v = 1 \text{ km s}^{-1}$ is adopted². Except for some pure rotational lines at submillimeter wavelengths, the HCN lines remain optically thin. The density for this spectrum is chosen high enough to thermalize the HCN levels so that vibrational levels with high critical densities are also populated.

The strongest bands of this spectrum are at 2.9–3.2 μm in the near-IR, at 6–8 μm and 11–18 μm in the mid-IR and at wavelengths $> 50 \mu\text{m}$ in the submillimeter. The near-IR feature consists of the 10^0_0 – 00^0_0 band, which is a factor of 10 stronger than 12^0_0 – 02^0_0 and 100 times stronger than 11^1_0 – 01^1_0 . These bands do not have a Q-branch ($\Delta J = 0$), since $\Delta l = 0$ ($\Sigma^+ \rightarrow \Sigma^+$). This is also the case in the 6–8 μm feature centered at 7.08 μm . The

² This intrinsic line width should not be confused with the observed, much broader line, resulting from the disk rotation.

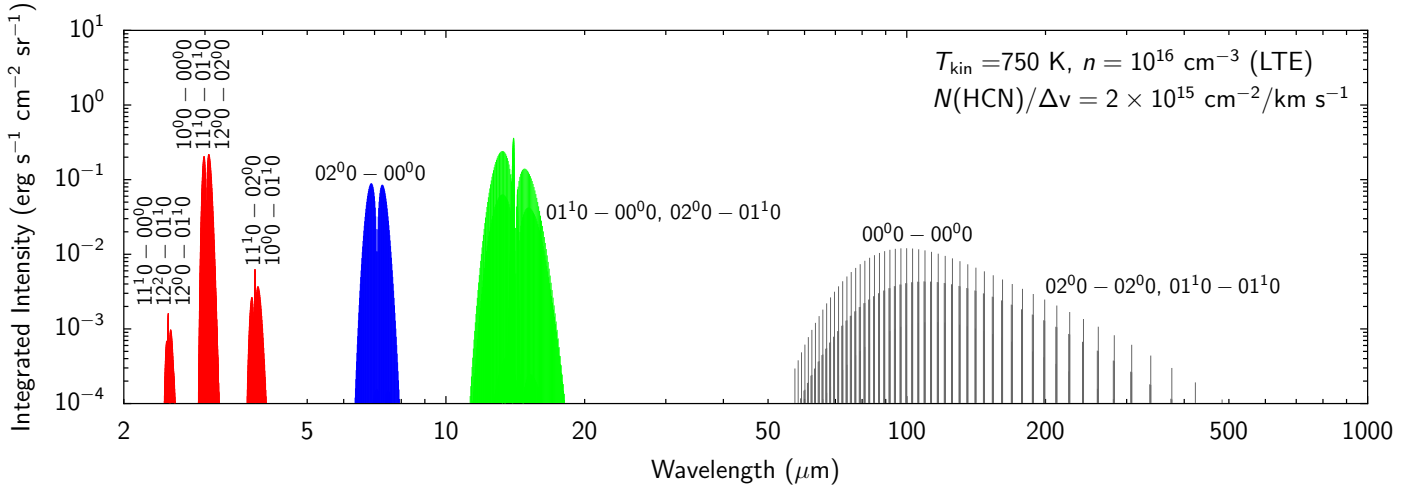


Fig. 2. HCN integrated intensity for a density of 10^{16} cm^{-3} , a kinetic temperature of 750 K and a HCN column density of $2 \times 10^{15} \text{ cm}^{-2}$ at a line width of $\Delta v = 1 \text{ km s}^{-1}$. For this density, the lines are close to the local thermal equilibrium (LTE). The same color scheme as in Figure 1 is used. Only the strongest bands are labeled.

11–18 μm feature centered at 13.95 μm has $\Delta l = 1$ ($\Pi \rightarrow \Sigma^+$) and thus a strong Q-branch. Pure rotational lines within the three vibrational ladders with the lowest energies (00^0_0 , 01^1_0 , and 02^0_0) contribute to the submillimeter lines. The l -type splitting shifts the ground states of the vibrational ladders by less than 0.5 GHz and thus cannot be seen in this spectrum (see Thorwirth et al. 2003).

2.3. Dependence on kinetic temperature, density and radiation field

The HCN excitation and line emission depends on kinetic temperature, collisional partner density and ambient radiation field. In Figure 3, full HCN spectra with varied parameters are compared. To study the temperature and collisional partner density, no external radiation field is included. The dependence on an external (continuum) radiation field is then studied by including a diluted black-body $\langle J_{\nu, \text{ext}} \rangle = WB_{\nu}(T_{\text{rad}})$ with $T_{\text{rad}} = 750 \text{ K}$. This T_{rad} has been adopted to reproduce the observed flux ratios towards AS 205 (N) (Sect. 2.4). The parameter range explored here approximately corresponds to the inner protoplanetary disk (Sect. 3). Typical detection limits for emission from the innermost region of a disk ($R = 1 \text{ au}$ at 100 pc) are shown for VLT-CRIRES and *Spitzer* (Salyk et al. 2011; Mandell et al. 2012). The detection limits scale as R^2 and four times weaker lines can be detected if $R = 2 \text{ au}$. For the far-IR lines within the wavelength range of *Herschel*-PACS (55–210 μm) the detection limit within $R = 50 \text{ au}$ at 100 pc is shown, corresponding to the emitting size found with PACS for other molecules (OH, H_2O , CO, see Fedele et al. 2013; Meeus et al. 2013).

Increasing the kinetic temperature from 250 to 1000 K yields higher intensities in almost all lines, most noticeably in the near-IR and high- J pure rotational transitions at submillimeter and far-IR wavelengths. This is because the shorter wavelength lines involve higher energy levels and the pure rotational ladder also extends up to several 1000 K for $J = 60$ (Figure 1). In the case of optically thin and thermalized lines, the emission is approximately $I \propto \exp(-E/kT)$ for an upper level energy E . At densities of 10^{12} cm^{-3} a temperature close to 1000 K is necessary to excite the IR lines sufficiently for a detection from the innermost 1 au of a protoplanetary disk.

Higher collisional partner densities help exciting the lines, bringing them close to thermalization. Levels are thermalized above the so-called critical density, defined as $n_{\text{crit}} = A_{ij}/K_{ij}$ for a two-level system. Below the critical density, optically thin emission is $I \propto n/n_{\text{crit}}$. For low- J pure rotational lines, critical densities are on the order of 10^8 cm^{-3} , e.g. for $J = 4 \rightarrow 3$. Thus, the pure rotational lines do not change considerably between densities of 10^9 cm^{-3} and 10^{15} cm^{-3} , because these lines are already thermalized. On the other hand, the 14 μm lines have critical densities on the order of a few times 10^{12} cm^{-3} and the 3 μm lines on the order of 10^{15} cm^{-3} . Thus, these bands only show considerable emission at very high densities in the context of protoplanetary disks.

Radiative pumping by a diluted black-body dominates over collisional excitation, if (e.g., Tielens 2005),

$$\frac{W}{\exp(h\nu/kT_{\text{rad}}) - 1} \gtrsim \frac{n}{n_{\text{crit}}} . \quad (3)$$

For the assumed $T_{\text{rad}} = 750 \text{ K}$ and a density of 10^9 cm^{-3} , radiation already dominates over collisions for $W \gtrsim 10^{-3}$ (14 μm) and $W \gtrsim 6 \times 10^{-4}$ (3 μm). However a stronger radiation field is necessary to produce detectable line emission in the near/mid-IR (Figure 3).

2.4. Comparison with observations

HCN lines both at 3 μm and 14 μm have been detected towards the T Tauri disk AS 205 (N) (northern component). Using the near-IR high-resolution ($R = \lambda/\Delta\lambda \sim 10^5$) spectrometer CRIRES on VLT, Mandell et al. (2012) detected several HCN lines in the 3 μm band. The 10^0_0 - 00^0_0 R(6) line has a flux of $4.7 \times 10^{-15} \text{ erg cm}^{-2} \text{ s}^{-1}$ at a calibration uncertainty of $\sim 30\%$. The lines have a low line-to-continuum ratio, thus the detection with CRIRES is very challenging. Not much information can be extracted from the line profile or spectro-astrometry and we will here focus on the total line flux. With the infrared spectrograph IRS onboard the *Spitzer Space Telescope*, Salyk et al. (2011) found a total flux of $(2.2 \pm 0.2) \times 10^{-13} \text{ erg cm}^{-2} \text{ s}^{-1}$ for the spectrally unresolved Q-branch at 13.7–14.1 μm .

For a first comparison of the non-LTE models with the observations, it is assumed that the 3 and 14 μm lines emerge from

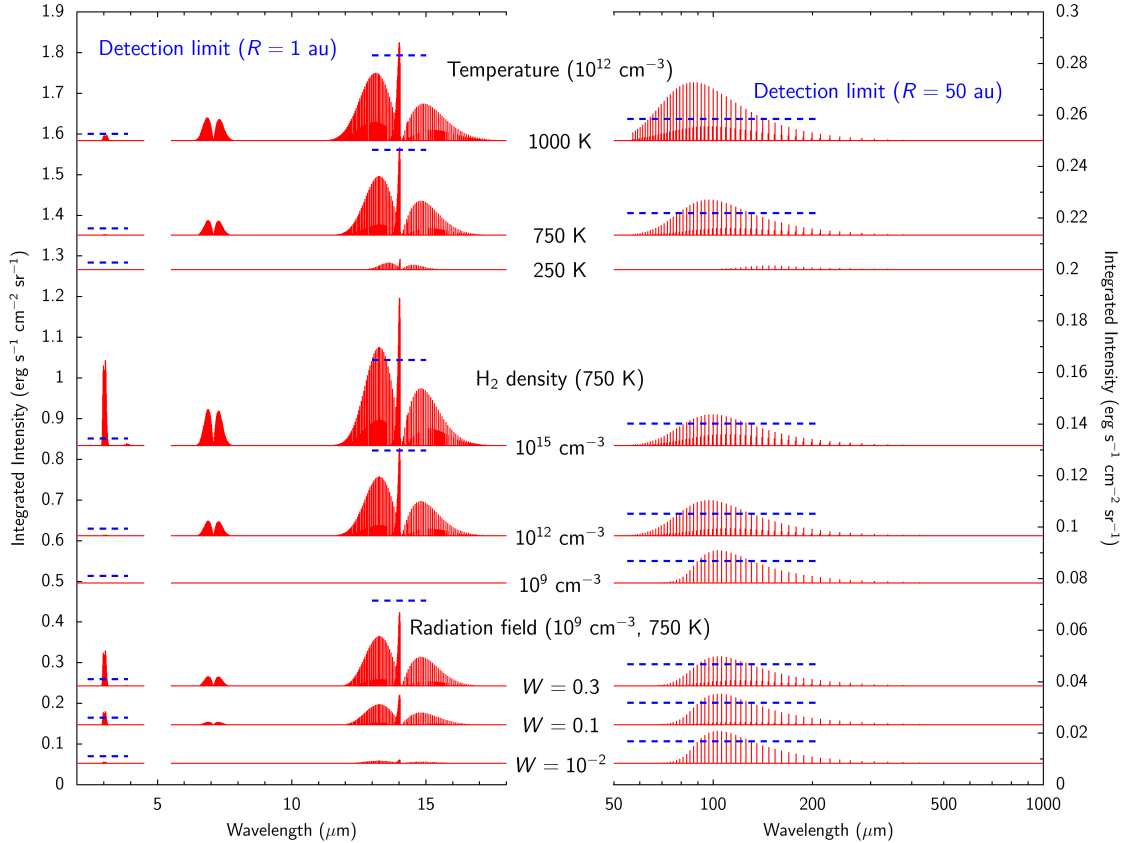


Fig. 3. HCN spectrum depending on kinetic temperature, density and radiation field for a slab model. The HCN column density is fixed to $2 \times 10^{15} \text{ cm}^{-2}$ and the line width to $\Delta v = 1 \text{ km s}^{-1}$. The intensity scales of the IR (2-18 μm) and far-IR/submillimeter portions of the spectrum are different. The blue dashed line shows the typical detection limit of CRILES and *Spitzer* assuming an emitting region with radius $R = 1 \text{ au}$. For *Herschel*-PACS, the detection limit within 50 au is shown.

the same region of the disk and we will thus restrict our comparison to line ratios. This is motivated by the fact, that the size of the emitting region is difficult to constrain from current observations and often the assumption is made that the emitting size of HCN is that same as for water (e.g., Salyk et al. 2011). We run RADEX models for densities between 10^7 and 10^{16} cm^{-3} . The kinetic temperature is fixed to 250, 500, 750, or 1000 K and the column densities to 10^{13} , 10^{15} , or 10^{17} cm^{-2} at an intrinsic line width $\Delta v = 1 \text{ km s}^{-1}$. These column densities cover the range of values derived from observations (Salyk et al. 2011; Carr & Najita 2011). Models with collisional excitation only or with additional radiation field from a 750 K blackbody diluted by $W = 0.1$ or $W = 0.01$ are explored.

Figure 4 shows the integrated intensity³ of the R(6) $10^0 - 00^0$ $3 \mu\text{m}$ line and the total $13.7 - 14.1 \mu\text{m}$ emission and compares their line ratios with observations. For the models without radiation field, the intensity of both $3 \mu\text{m}$ and $14 \mu\text{m}$ lines increases linearly with density up to about their respective critical densities when they thermalize. Models with a pumping radiation field yield considerable emission even for low densities. For these models, the intensity increases with density only for the warm models (750 and 1000 K) since collisions thermalize the lines to a higher temperature than the radiation field. Thus, collisions may also decrease the line intensity. The increase of line intensity with radiation field (W) is about linear at low densi-

ties much below the critical densities of the transitions. In the limit of low densities, the radiation field thermalizes the level population to the temperature T_{rad} . In the limit of high densities, collisions thermalize the level population to the kinetic temperature. Thus, in this example with $T_{\text{rad}} = 750 \text{ K}$, the line ratios are driven to the same value ($\sim 2 \times 10^{-2}$) at low densities as they are at high densities in the panel for the kinetic temperature of 750 K. A lower/higher T_{rad} would decrease/increase the line ratio. For high column densities (10^{17} cm^{-2}), the $14 \mu\text{m}$ lines get optically thick first, and the line ratio is increased compared to the optically thin case for the same kinetic temperature.

The comparison of the modeled and observed line ratios shows that pure collisional excitation requires very high densities $> 10^{13} \text{ cm}^{-2}$ at kinetic temperatures $> 750 \text{ K}$. Meanwhile, a diluted radiation field with $T_{\text{rad}} = 750 \text{ K}$ can easily reproduce the observed line ratio, as long as the density is low enough to not affect the $14 \mu\text{m}$ lines which have a lower critical density.

3. HCN emission from protoplanetary disks

More insight into the excitation and line formation process can be gained through models of protoplanetary disks including a realistic geometry. Such models have a range of physical conditions and not a single temperature and density as the slab models presented before. Using full disk models the size and location of the emitting regions can be constrained and effects of continuum shielding or radial/vertical variations in the abundance structure accounted for. This is not a trivial issue to calculate, since the pumping IR continuum that is mainly formed in the inner hot

³ Scaled to flux in $\text{erg s}^{-1} \text{ cm}^{-2}$ by multiplying with the solid angle $2.35 \times 10^{-11} (R[\text{au}]/D[\text{pc}])^2 \text{ sr}$, where R is the radius of the emitting region in au and D the distance to the object in parsec.

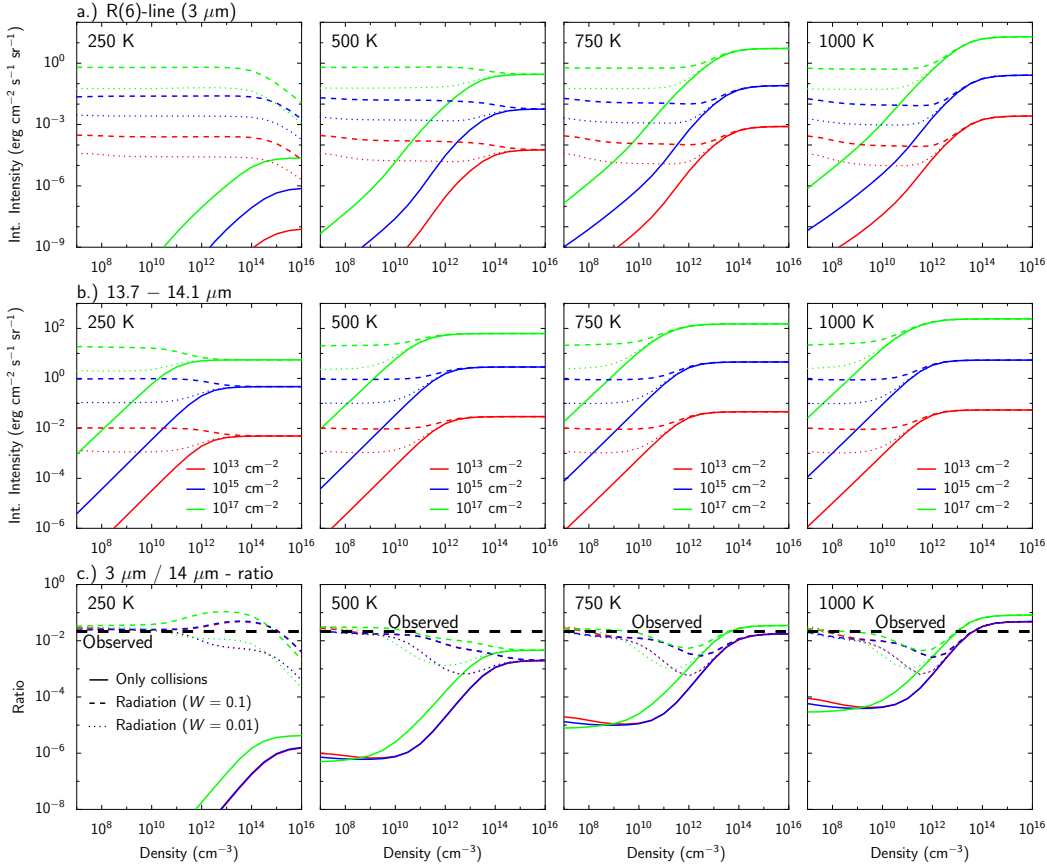


Fig. 4. Results of slab models. **a)** Integrated intensity of the R(6) $10^0 - 00^0$ line depending on the density for different kinetic temperatures and column densities. Solid lines show models that only consider collisions, while dashed and dotted lines represent models with a pumping radiation field of a 750 K blackbody diluted by $W = 0.1$ (dashed line) or $W = 0.01$ (dotted line). Red, blue, and green lines show results for column densities of 10^{13} cm^{-2} , 10^{15} cm^{-2} , and 10^{17} cm^{-2} , respectively. **b)** Total integrated intensity of all HCN lines between 13.7 and 14.1 μm for the same parameters as panel a). **c)** Ratio of panels a) and b) compared to the observed ratio towards AS 205 (N).

region, needs to be calculated at every position of the disk. Also, the molecular excitation needs to be calculated on a high resolution grid. In this section, we model the R(6) $10^0 - 00^0$ 3 μm line and 13.7–14.1 μm emission from AS 205 (N).

The model and its parameters are first introduced, the excitation of one particular model is presented and the effects of various parameters then studied. We emphasize that given the uncertainties in various input parameters (e.g., physical structure, dust opacities, ...), it is not the goal of this work to yield a perfect fit to the observed data, but to study the relative importance of different processes and parameters, which are also of relevance for disks other than AS 205 (N).

3.1. Model setup

Part of the physical-chemical model DALI (**D**ust and **L**ines) is used in this work. Details of the model and benchmark tests are reported in Bruderer et al. (2012) and Bruderer (2013). Starting from a gas and dust density structure, the Monte-Carlo radiative transfer module calculates the dust temperature and the local continuum radiation field at each position of the disk. Then, the excitation module yields the HCN level population at all positions. The local radiation field is obtained using an escape probability approach (Appendix A.2 in Bruderer 2013) accounting for both line and continuum contributions. For the continuum pumping, the radiation field obtained by the continuum radiative transfer module, shielded by the line opacity, is used. Finally, synthetic spectra are derived with the raytracing module, which solves the radiative transfer equation along rays through the disk. The approach used here is akin to Meijerink et al. (2009) and Thi et al. (2013) used for H_2O and CO, respectively. However, unlike Thi et al. (2013) a parameterized abundance structure is

used instead of chemical network results. This allows us to study the excitation effects independently of uncertainties in the HCN chemistry. The assumption of $T_{\text{gas}} = T_{\text{dust}}$ will not affect the results, as HCN has very high critical densities and $T_{\text{gas}} \sim T_{\text{dust}}$ in regions where collisions are important.

The main input parameters for the AS 205 (N) model are taken from Andrews et al. (2009). They have simultaneously fitted SED and submillimeter images using a parameterized physical structure with surface density profile

$$\Sigma(R) = \Sigma_c \left(\frac{R}{R_c} \right)^{-\gamma} \exp \left[- \left(\frac{R}{R_c} \right)^{2-\gamma} \right] \quad (4)$$

and vertical distribution

$$\rho(R, \theta) = \frac{\Sigma(R)}{\sqrt{2\pi} R h(R)} \exp \left[- \frac{1}{2} \left(\frac{\pi/2 - \theta}{h(R)} \right)^2 \right], \quad (5)$$

with the scale height angle $h(R) = h_c (R/R_c)^\psi$. The values of the parameters and other basic properties adopted are summarized in Table 1.

The abundance structure of HCN is either constant or a jump (Figure 5a) with a higher abundance in the hot FUV shielded inner disk (x_{in}) and the outer disk (x_{out}). In dense PDR models (e.g., Meijerink & Spaans 2005), HCN is abundant at $A_V > 2$ and temperatures above $T_{\text{jump}} = 200 \text{ K}$. We thus define the inner region by these two conditions, and later study the effect of changing the temperature threshold. Excitation effects are first studied with constant abundance models ($x_{\text{in}} = x_{\text{out}}$), before models with a jump in abundance are presented. The models include both thermal and turbulent broadening (FWHM $\sim 0.1 \text{ km s}^{-1}$). Thermal broadening dominates in regions where the 3 μm and 14 μm emission emerges from.

Table 1. Adopted basic data of AS 205 (N).

Parameter		Value
Star		
Mass	$M_* [M_\odot]$	1.0 ^(a)
Luminosity	$L_* [L_\odot]$	4.0 ^(a)
Effective Temperature	$T_{\text{eff}} [\text{K}]$	4250 ^(a)
Disk		
Disk mass	$M_{\text{disk}} [M_\odot]$	0.029 ^(a,d)
Surface density index	γ	0.9 ^(a)
Characteristic radius	$R_c [\text{au}]$	46 ^(a)
Inner radius	$R_{\text{in}} [\text{au}]$	0.14 ^(a)
Scale height index	ψ	0.11 ^(a)
Scale height angle	$h_c [\text{rad}]$	0.18 ^(a)
Dust properties ^(e)		
Size	$a [\mu\text{m}]$	0.005 – 1000 ^(a)
Size distribution		$dn/da \propto a^{-3.5(a)}$
Composition		ISM ^(a,b)
Distance	$d [\text{pc}]$	125 ^(c)
Inclination	$i [^\circ]$	20 ^(c)

Notes. ^(a) Andrews et al. (2009), ^(b) Draine & Lee (1984); Weingartner & Draine (2001), ^(c) Pontoppidan et al. (2011), ^(d) Assuming a gas-to-dust ratio of 100, ^(e) See Online Figure A.1

The gas-to-dust (“G/D”) ratio is increased from the standard ratio of G/D=100 in some of the models, while the dust structure is kept the same for all models. As discussed in Meijerink et al. (2009), a higher gas-to-dust ratio leads to less dust absorption for high density gas. Thus, the line photosphere ($\tau_{\text{line}} = 1$) is shifted vertically upwards with respect to the dust photosphere ($\tau_{\text{dust}} = 1$) for an increased gas-to-dust ratio resulting in a higher line-to-continuum ratio. While we change the gas-to-dust ratio globally for the model, it does not mean that the disk gas mass changes by the same factor because an increased gas-to-dust ratio can be taken as a proxy for dust settling (Meijerink et al. (2009)) and the IR lines trace only the inner part of the disk, while the bulk of the disk mass is in the outer disk.

Initially, large grains (0.005 μm - 1 mm) including grain growth are used, as adopted in the SED/image fitting by Andrews et al. (2009). In Section 3.4 the effect of smaller, ISM like, grains is studied. Similar to the gas-to-dust ratio, changing the dust opacity also varies the position of the dust photosphere ($\tau_{\text{dust}} = 1$) and the two effects are thus expected to be somewhat degenerate.

3.2. The excitation mechanism of HCN

The relative importance of excitation processes and formation of the R(6) 10⁰ – 00⁰ 3 μm and Q(6) 01¹0 – 00⁰ 14 μm lines is discussed with a model having a gas-to-dust ratio of 1000 and $x_{\text{in}} = x_{\text{out}} = 3 \times 10^{-8}$. This model fits both the 3 μm CRIRES and the 14 μm *Spitzer* observations reasonably well (Table 2).

Figure 5a shows the density structure and Figure 5b the temperature structure of the model. Densities up to a few times 10¹⁶ cm⁻³ are reached in the inner midplane. The temperature spreads from ~ 10 K in the outer midplane up to the dust sublimation temperature of ~ 1500 K in the inner disk. Thus, there are region in the disk with a sufficiently high temperature and density to excite the HCN vibrational band collisionally, but these may be buried below the dust photosphere.

The vertical optical depth of the continuum and the line are indicated in Figures 5d-5i by blue and red lines. The blue lines show the depth where the continuum gets optically thick ($\tau_{\text{dust}} =$

1) and the red lines where the HCN line does so ($\tau_{\text{line}} = 1$ at the line center). The black line indicates the height where the critical density of the transition is reached ($n > n_{\text{crit}}$). Both of the 3 μm and 14 μm lines become saturated above the $\tau_{\text{dust}} = 1$ region, with peak line optical depth of about a few (3 μm) and ~ 30 (14 μm). The region where the 3 μm line is collisionally excited is entirely below $\tau_{\text{dust}} = 1$. For the 14 μm line the critical density is reached higher in the disk and above the $\tau_{\text{dust}} = 1$ in the inner 2 au. Thus, collisional excitation does not affect the 3 μm line but may affect the 14 μm line.

Radiative pumping is studied in Figures 5d and 5g by the dilution factor relative to a $T_{\text{rad}} = 750$ K blackbody. Compared to the results in Section 2.3 (Figure 3) where it is found that $W \sim 0.1 - 0.3$ are necessary for a detection within a region of $R = 1$ au, the dilution factors are found to be lower. However, emitting regions out to 10 au are a factor of 100 larger and $W \sim 0.001$ can produce a considerable line emission since it approximately scales with W (Figure 4). In fact, most of the IR continuum photons are produced in the innermost part of the disk and the continuum intensity in the upper disk decreases roughly as $\sim r^{-2}$, while the emitting region increases as $\sim r^2$. We may thus expect to find radiatively pumped molecules out to considerable distances. The HCN lines are seen in emission because the pumping photons are produced in the innermost part, while the radiatively excited molecules are mostly farther out and not in front of the continuum. This thus corresponds to the situation of *resonant scattering*.

The excitation temperature⁴ T_{ex} of the two lines is shown in Figures 5e and 5h. As a result of the strong radiation field, $T_{\text{ex}} > T_{\text{dust}}$ for most regions of the disk. Close to the midplane, in the region with $n > n_{\text{crit}}$, the lines are thermalized by collisions and $T_{\text{ex}} \sim T_{\text{dust}}$. Both lines are thus excited out to large radii and regions beyond the innermost 1 au may contribute considerably to the emission.

Regions with the largest contribution to the lines are given in Figures 5f and 5i. Indicated is the region which contributes 50 or 75 % of the observable line. Thus, most of the 3 μm line emerges from radial distances between the inner edge of the disk at 0.14 au and ~ 10 au. The 14 μm line emerges predominantly from about 1 – 15 au, since the emission within the innermost 1 au cannot compete with the larger emitting region farther out. In the vertical direction, the emission of both lines is concentrated close to the $\tau_{\text{line}} = 1$ surface. Thus, the 14 μm emission also emerges mostly from regions with densities below the critical density, and radiative pumping dominates as for the 3 μm line.

We conclude that radiative pumping is the major excitation mechanism for both the 3 μm and 14 μm lines studied here. As the size of the emitting region and geometrical dilution of the pumping IR field approximately balance out, the lines can be excited out to considerable distances on the order of 10 au. This is much larger than previous estimates of the emitting region based on LTE models and/or other molecules like water (~ 2.1 au for 14 μm by Salyk et al. 2011 and < 1 au for 3 μm by Mandell et al. 2012).

3.3. LTE versus non-LTE

An important goal of this work is to find the bias in abundance determination introduced by the LTE assumption. In Figure 6, the line flux of the R(6) 10⁰ – 00⁰ line at 3 μm and the total emission between 13.7 and 14.1 μm of non-LTE models

⁴ Defined by $n_i/n_j = g_i/g_j \exp(-\Delta E/kT_{\text{ex}})$, with the level population $n_{i,j}$, the statistical weights $g_{i,j}$ and the energy difference ΔE .

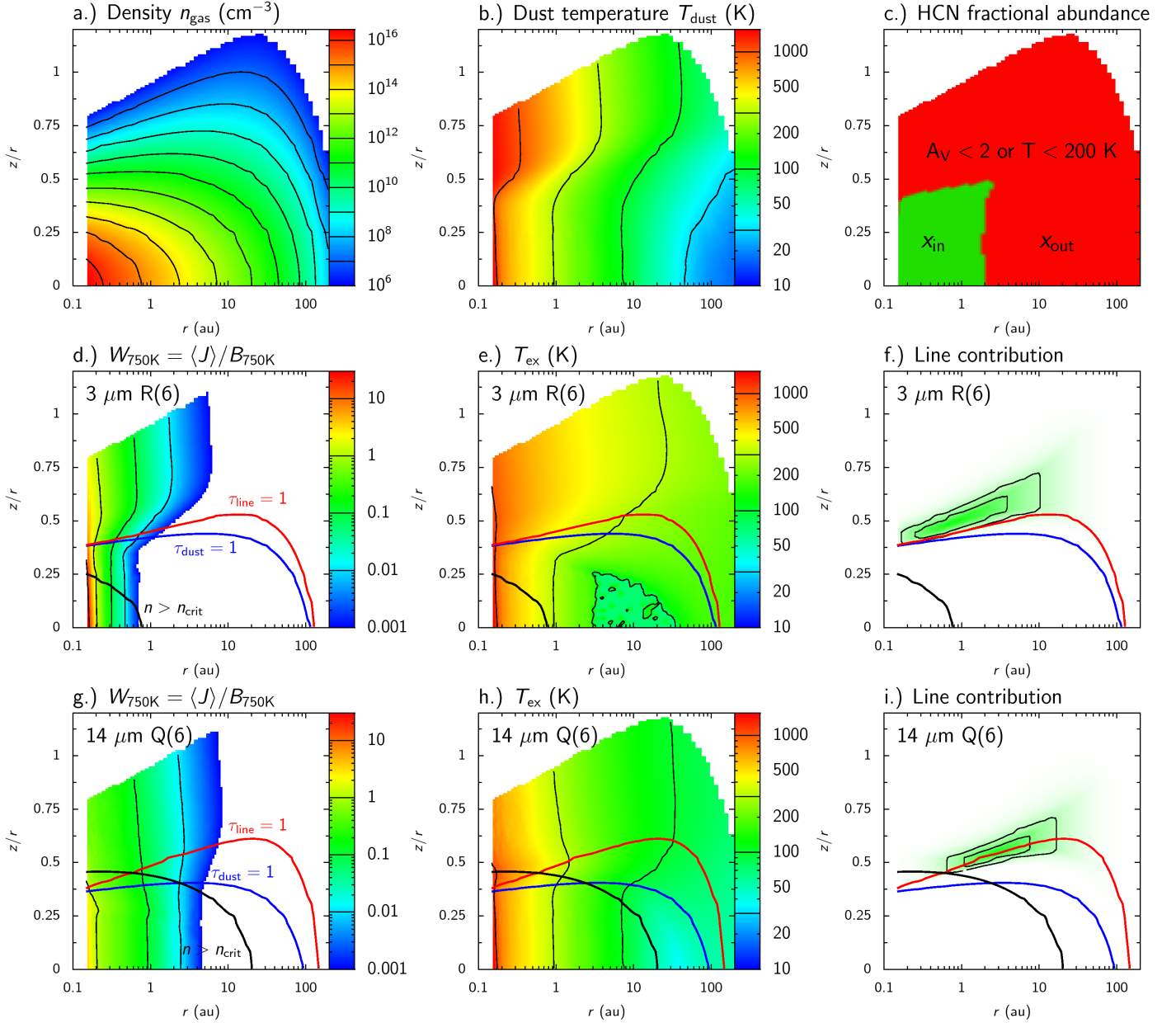


Fig. 5. Parameters of the AS 205 (N) model compared to the formation of the R(6) 10^0-00^0 line at $3\ \mu\text{m}$ and Q(6) 01^1-00^0 line at $14\ \mu\text{m}$. The model with a gas-to-dust ratio of 1000 and a constant abundance $x_{\text{in}} = x_{\text{out}} = 3 \times 10^{-8}$ is shown. **a)** Density structure. **b)** Dust temperature. **c)** Adopted fractional abundance of HCN. **d)** Continuum radiation field relative to a 750 K blackbody for the R(6) $3\ \mu\text{m}$ line. Overlaid are the $\tau = 1$ surface of the line (red) and continuum (blue) and the region where the critical density of the line is reached (black). **e)** Excitation temperature of the R(6) $3\ \mu\text{m}$ line. **f)** Regions with 50 or 75 % contribution to the observed flux. **g)-i)** As panels d)-f), but for the Q(6) $14\ \mu\text{m}$ line.

with varied HCN fractional abundance⁵ and gas-to-dust ratio are compared to LTE models.

Somewhat surprisingly, the $3\ \mu\text{m}$ line of the non-LTE model is stronger by a factor of up to ~ 3 compared to the LTE model. This is understood by the radiative pumping, which can excite the line superthermally ($T_{\text{ex}} > T_{\text{dust}}$) out to large radii of ~ 10 au. For the observed flux, the HCN abundance determined with a LTE model from the $3\ \mu\text{m}$ line would be a factor of 3 too high. For the $14\ \mu\text{m}$ total flux, the difference between non-LTE and LTE model are mostly smaller than for the $3\ \mu\text{m}$ line ($<$ factor 2). As a result of the higher optical depth of the $14\ \mu\text{m}$ line

compared to the $3\ \mu\text{m}$ line, the curve flattens off for higher abundance. At high HCN abundance, the lines cross and LTE models yield higher fluxes than the non-LTE model. This is understood by the τ_{line} surface shifting to the upper disk for higher abundances. In that region, the $14\ \mu\text{m}$ lines are slightly subthermally excited ($T_{\text{ex}} < T_{\text{dust}}$) as comparison of Figure 5h with 5b shows. The abundance determined from the $14\ \mu\text{m}$ flux is almost unaffected by the LTE assumption.

The gas-to-dust ratio and the HCN abundance are degenerate, which means that a factor of ten higher abundance but a factor of ten lower gas-to-dust ratio, resulting in the same total number of HCN molecules, yields almost the same flux (and line-to-continuum ratio). This would be different if collisional

⁵ Relative to the total gas density.

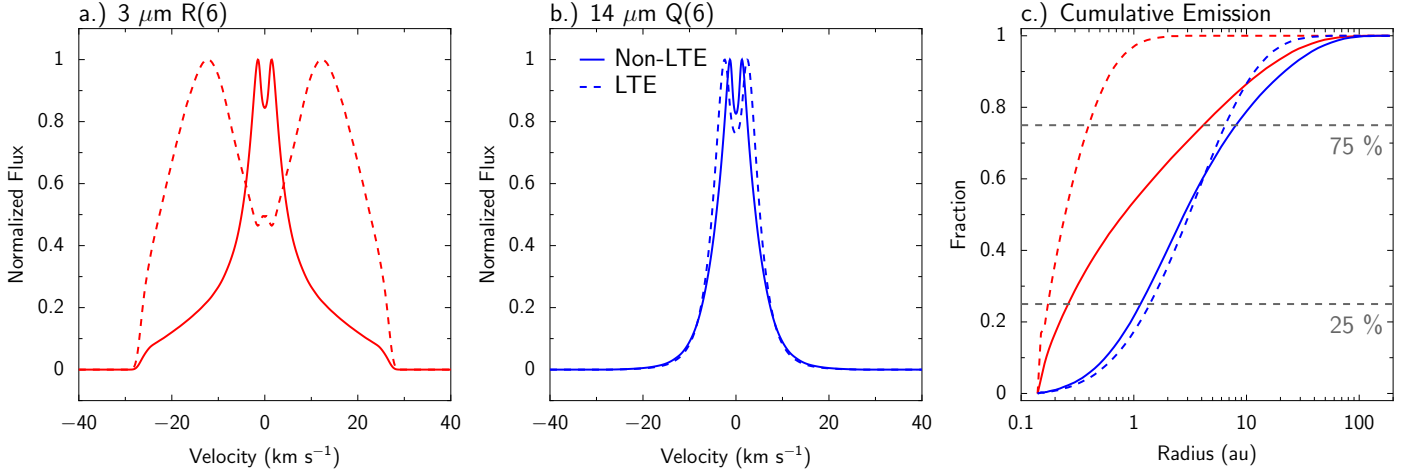


Fig. 7. Spectrum of the **a)** R(6) $10^0 - 00^0$ line at $3 \mu\text{m}$ and **b)** Q(6) $01^{10} - 00^0$ line at $14 \mu\text{m}$ of the AS 205 (N) model with a gas-to-dust ratio of 1000 and a constant abundance of $x_{\text{in}} = x_{\text{out}} = 3 \times 10^{-8}$. **c)** Contribution to the line flux within a certain radius. Results from the non-LTE and LTE model are shown in solid and dashed lines, respectively.

pumping is important for the excitation, because models with a high gas-to-dust ratio would then yield stronger lines due to the higher collisional partner density. Here, it means that the fractional abundance of HCN can only be determined relative to a gas-to-dust ratio. To detect lines, the line-to-continuum ratio can be the limiting factor (Appendix C).

The line profiles of a LTE and non-LTE model with a gas-to-dust ratio of 1000 and $x_{\text{in}} = x_{\text{out}} = 3 \times 10^{-8}$ are compared in Figure 7. Also shown is the cumulative contribution to the flux within a certain radius. In the non-LTE model, both the $3 \mu\text{m}$ and $14 \mu\text{m}$ lines are narrow and peaky, with the $3 \mu\text{m}$ line having a broad component extending out to the maximum velocity of $\sim 27 \text{ km s}^{-1}$. The peaky line profiles result from the large emitting regions of both lines, as the cumulative emission shows. The LTE models produce a much broader $3 \mu\text{m}$ line, while the $14 \mu\text{m}$ line is similar to the non-LTE model. The cumulative emission again reflects this. While similar regions contribute to the $14 \mu\text{m}$ emission in the LTE and non-LTE model, a much smaller region contributes in the LTE model to the $3 \mu\text{m}$ line. This is due to the larger upper level energy of the $3 \mu\text{m}$ line compared to the $14 \mu\text{m}$ line.

3.4. Dependence on dust properties

The degeneracy between the gas-to-dust ratio and molecular abundance, found in the previous section, shows that the total amount of visible HCN molecules determines the flux. Visible means that the molecules need to be above the dust photosphere. How does a change in grain opacity affect the lines? For comparison, we adopt the dust opacities by Mulders et al. (2011) for a size distribution of $0.1\text{-}1.5 \mu\text{m}$ instead of the $0.005 \mu\text{m} - 1 \text{ mm}$ large/grown grains used by Andrews et al. (2009). Mulders et al. (2011) have used those opacities to fit the SED and images of HD 100546, a Herbig Be transitional disk. The smaller grains have an IR absorption similar the ISM grains, with an increased extinction opacity by a factor of 10 at $3 \mu\text{m}$ and 2.5 at $14 \mu\text{m}$ compared to the large grains (Online Figure A.1). While the models with changed dust opacity do not fit the AS 205 (N) SED anymore, they are illustrative to study the effects.

The fluxes of the $3 \mu\text{m}$ $10^0 - 00^0$ R(6) and total $13.7\text{-}14.1 \mu\text{m}$ emission for non-LTE models with both grain opacities are shown in Figure 8. The $3 \mu\text{m}$ lines scale almost exactly with

the difference in the dust opacity. The $14 \mu\text{m}$ flux on the other hand, is scaled by a slightly smaller factor than the change in dust opacity, because of line opacity effects. Both the absolute fluxes and the $3 \mu\text{m}$ to $14 \mu\text{m}$ flux ratios are thus affected by the dust opacities. Thus, while changes in the dust opacities overall affect the line fluxes in a similar way as the gas-to-dust ratio, they may also change the ratios between vibrational bands. Here, the $14 \mu\text{m} / 3 \mu\text{m}$ flux ratios (Table 2) are increased by a factor of ~ 3 to 6, away from the observed value.

3.5. The effect of different abundance structures

Chemical models suggest that the HCN abundance is increased in the hot inner 1-2 au, due to a warm and hot-core like chemistry (Lahuis & van Dishoeck 2000; Doty et al. 2002; Agúndez et al. 2008; Bast et al. 2013). Non-LTE models with varying both inner (x_{in}) and outer abundance (x_{out}) are run to test the effects of such a “jump abundance” profile. In Figure 9, the $3 \mu\text{m}$ R(6) line flux and the total $14 \mu\text{m}$ emission is shown depending on the inner abundance and for different gas-to-dust ratios. The outer abundance is scaled such that the total number of HCN molecule in that region is the same for the three gas-to-dust ratios. Thus, the outer abundance is $x_{\text{out}} = 10^{-9..-7}$ for G/D= 100 but $x_{\text{out}} = 10^{-11..-9}$ for G/D= 10000.

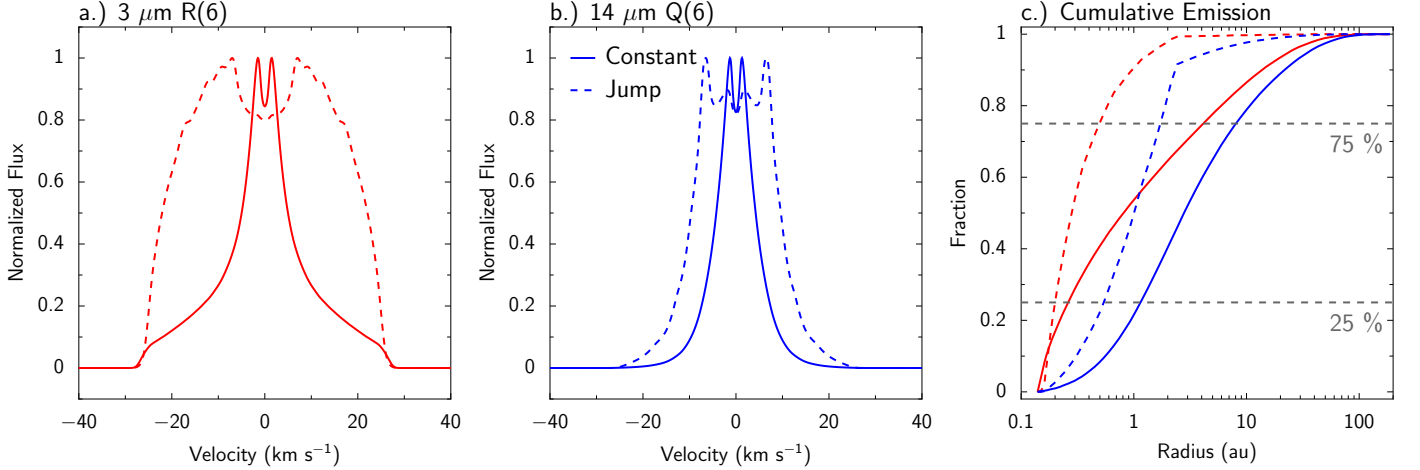
The $3 \mu\text{m}$ lines depend more on the inner abundance than the $14 \mu\text{m}$ flux, due to the lower line optical depth and smaller emitting region. For the highest inner abundance of each gas-to-dust ratio, most of the emission at both 3 and $14 \mu\text{m}$ emerges from the inner region ($< 2 \text{ au}$), since the line fluxes do not change much with x_{out} anymore.

For both a gas-to-dust ratio of 10000 (with $x_{\text{in}} = 10^{-7}$ and $x_{\text{out}} = 10^{-10}$) and a gas-to-dust ratio of 1000 (with $x_{\text{in}} = 3 \times 10^{-7}$ and $x_{\text{out}} = 10^{-9}$), the observed fluxes can be reproduced well (Table 2). No combination of x_{in} and x_{out} can be found to equally well reproduce both fluxes when the gas-to-dust ratio is set to 100. This is because of the lower density for lower gas-to-dust ratios in the inner 2 au close to the $\tau_{\text{dust}} = 1$ surface. The densities in that region are above the critical density for higher gas-to-dust ratios as Figure 5 shows. Thus, in the situation where most of the $14 \mu\text{m}$ emission emerges from the inner most region due to the chemical abundance structure, collisional excitation

Table 2. Fluxes of the R(6) $10^0 - 00^0$ line at $3 \mu\text{m}$ and the total HCN emission between 13.7 and 14.1 for AS 205 (N) models with a constant or jump abundance compared to observations.

Abundance profile	T_{jump} [K]	G/D ratio	x_{in}	x_{out}	$3 \mu\text{m}$ [erg s $^{-1}$ cm $^{-2}$]	$14 \mu\text{m}$ [erg s $^{-1}$ cm $^{-2}$]	Flux ratio $14 \mu\text{m} / 3 \mu\text{m}$
Constant	-	1000	3(-8)	3(-8)	3.3(-15)	3.8(-13)	115
Jump	200	1000	3(-7)	1(-9)	4.7(-15)	2.4(-13)	51
Jump	200	10000	1(-7)	1(-10)	4.6(-15)	2.3(-13)	50
Jump	300	1000	6(-7)	1(-10)	6.0(-15)	1.6(-13)	27
Jump	300	10000	6(-7)	1(-11)	4.4(-15)	2.0(-13)	45
Observed					4.7(-15)	2.2(-13)	46

Notes. $a(b)$ means $a \times 10^b$


Fig. 10. Spectrum of the **a)** R(6) $10^0 - 00^0$ line at $3 \mu\text{m}$ and **b)** Q(6) $01^{10} - 00^0$ line at $14 \mu\text{m}$ of the AS 205 (N) model with constant abundance ($G/D= 1000$ and $x_{\text{in}} = x_{\text{out}} = 3 \times 10^{-8}$, solid lines) or with jump abundance ($G/D= 1000$, $x_{\text{in}} = 3 \times 10^{-7}$, and $x_{\text{out}} = 1 \times 10^{-9}$, dashed lines). **c)** Contribution to the line flux within a certain radius.

can become important. Consequently, the degeneracy between gas-to-dust ratio and HCN abundance is broken.

Most of the emission in the well-fitting jump abundance models is from the innermost 2 au, because of the large jump in abundance. This is unlike the constant abundance models with emission out to ~ 10 au. The effect of the different emitting regions on the line profile is shown in Figure 10. As expected, both the $3 \mu\text{m}$ and $14 \mu\text{m}$ lines from the jump abundance models are much broader compared to the constant abundance models. The cumulative emission panel indeed confirms that the emission is much more centered in both lines and almost the entire emission of the $3 \mu\text{m}$ line and 75 % of the $14 \mu\text{m}$ line emerges from inside 2 au. While the line shape of the $3 \mu\text{m}$ line with jump abundance (Figure 10) and LTE excitation (7) are somewhat similar, one is the result of the abundance structure and the other of the excitation.

3.6. The size of the inner region

So far, we have assumed that the inner abundance extends out to regions with $T > T_{\text{jump}} = 200$ K. Increasing T_{jump} leads to a smaller, but warmer, emitting region. To illustrate the effect, we show models with $T_{\text{jump}} = 300$ K in Table 2. To still fit the observed line fluxes, the inner abundance needs to be increased, while the outer abundance lowered. Since the emitting region is warmer, the rotational temperature of the lines is higher, as it is mostly determined by collisional excitation of the vibrational ground state.

Figure 11 compares the *Spitzer* HCN features of the Q-branches of the $01^{10} - 00^0$ ($14.05 \mu\text{m}$) and $02^{00} - 01^{10}$ ($14.3 \mu\text{m}$) bands to three models convolved to the *Spitzer* spectral resolving power of $R \sim 600$. Data by the c2d legacy program is used (Lahuis et al. 2006; Evans et al. 2009). Models with $G/D= 1000$ and constant abundance or jump abundance with varied T_{jump} are shown. Also shown are models with a contribution of H^{13}CN included. These models are calculated assuming $60 = [^{12}\text{C}]/[^{13}\text{C}]$. Unfortunately, both HCN features overlap with water lines. Thus, the best fit water model by Salyk et al. (2011) is subtracted before comparison.

We find that the Q-branch at $14.05 \mu\text{m}$ is best reproduced by the model with $T_{\text{jump}} = 300$ K, however some residuals at around $14.0 \mu\text{m}$ remain, possibly because of an overcorrection of the water emission. The $02^{00} - 01^{10}$ Q-branch at $14.3 \mu\text{m}$ is stronger in the models with jump abundance and overproduces observations for $T_{\text{jump}} = 300$ K. While a model with jump abundance seems to fit observations better, none of the models can well reproduce both Q-branches. The comparison is however hampered by uncertainties in the correction for water emission. Interestingly, the red wing of the $14.05 \mu\text{m}$ Q-branch is better reproduced in the models with H^{13}CN included.

4. Discussion

4.1. Excitation and line formation effects

Owing to the very high critical densities of the HCN rovibrational lines, it could be expected that the lines are subther-

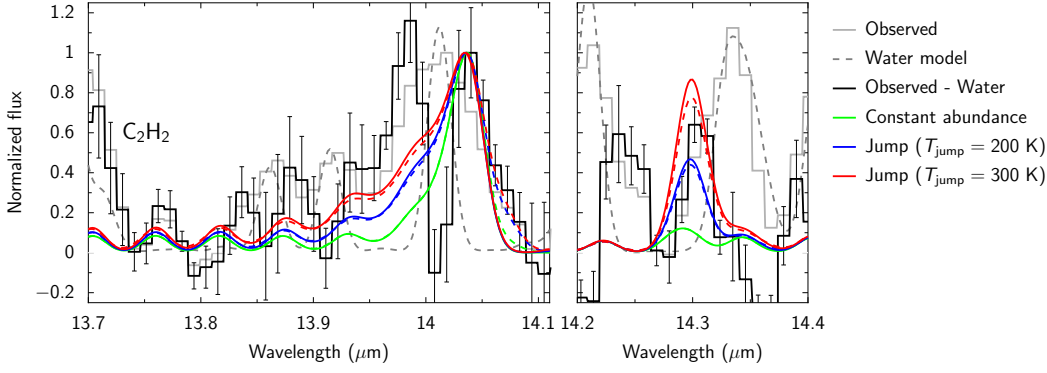


Fig. 11. *Spitzer* observations compared to the models given in Table 2 with $G/D=1000$ and constant or jump abundance. Dashed color lines show models including H^{13}CN . Gray lines show the observed spectrum and the best-fit water model by Salyk et al. (2011). The black line indicates the water subtracted spectrum. The spectra are normalized to the peak of the Q-branch at around $14.05 \mu\text{m}$.

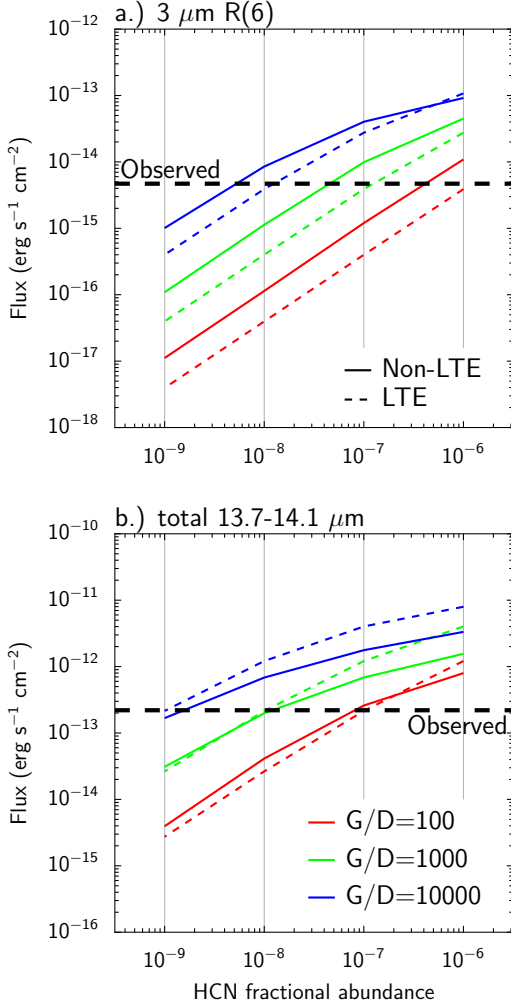


Fig. 6. Non-LTE and LTE results of the AS 205 (N) model for the **a)** $\text{R}(6) 10^0 - 00^0$ line at $3 \mu\text{m}$ and **b)** the total HCN emission between 13.7 and $14.1 \mu\text{m}$. The HCN fractional abundance is constant in the disk ($x_{\text{in}} = x_{\text{out}}$) and varied between 10^{-9} and 10^{-6} . Three different gas-to-dust (G/D) ratios of 100 (red), 1000 (green), and 10000 (blue) are shown. Non-LTE results are shown in solid, LTE results in dashed line. The fluxes observed by Salyk et al. (2009) ($14 \mu\text{m}$) and Mandell et al. (2012) ($3 \mu\text{m}$) are given in black dashed lines.

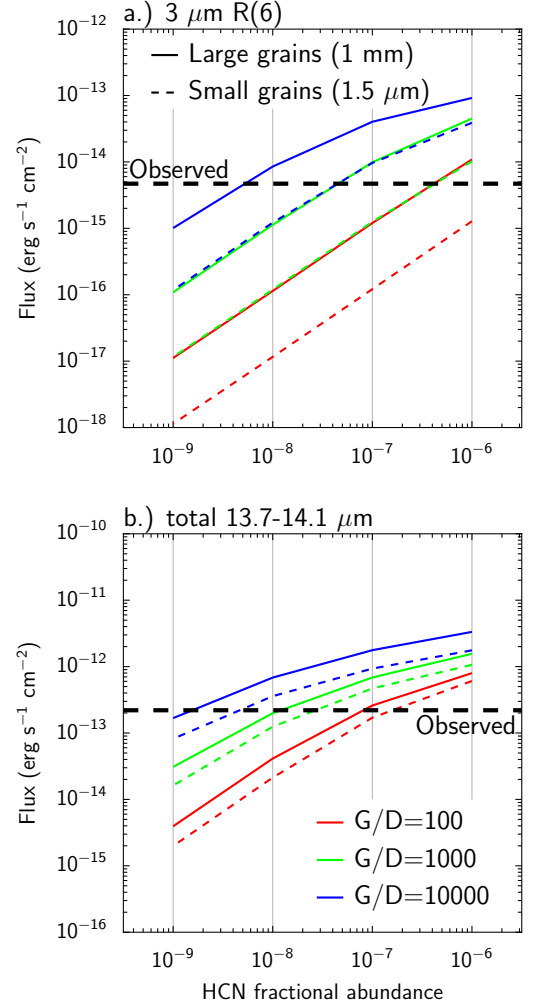


Fig. 8. Non-LTE results of the AS 205 (N) model comparing results with large grains (solid line) to ISM grains (dashed line). **a)** $\text{R}(6) 10^0 - 00^0$ line at $3 \mu\text{m}$ and **b)** the total HCN emission between 13.7 and $14.1 \mu\text{m}$. The adopted opacities are shown in Figure A.1. The HCN fractional abundance is constant in the disk ($x_{\text{in}} = x_{\text{out}}$) and varied between 10^{-9} and 10^{-6} . Three different gas-to-dust (G/D) ratios of 100 (red), 1000 (green), and 10000 (blue) are shown. The fluxes observed by Salyk et al. (2009) ($14 \mu\text{m}$) and Mandell et al. (2012) ($3 \mu\text{m}$) are given in black dashed lines.

mally excited, resulting in large differences in the abundance determined by LTE or non-LTE models. However, since infrared pumping provides an additional way of exciting the molecules, we find that the fluxes between LTE and non-LTE models do

not differ by more than a factor of few and consequently the abundance determination using LTE or non-LTE models is only affected by about the same factor. However, the line profiles be-

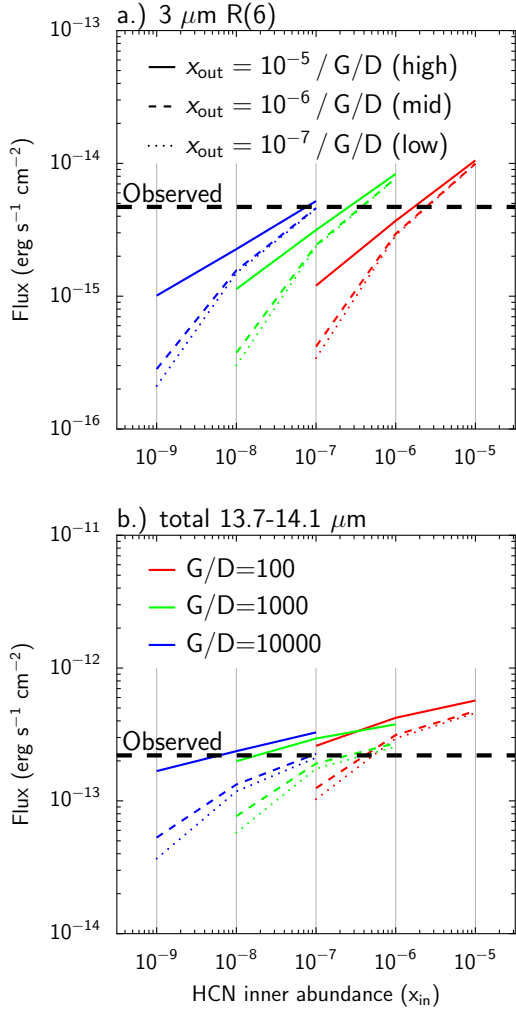


Fig. 9. Non-LTE results of the AS 205 (N) model comparing different abundances inside (x_{in}) and outside (x_{out}). **a)** R(6) $10^0 - 00^0$ line at $3 \mu\text{m}$ and **b)** the total HCN emission between 13.7 and $14.1 \mu\text{m}$. The outer abundance is scaled for the gas-to-dust ratio (G/D) and takes 3 different values (e.g., 10^{-9} , 10^{-8} , and 10^{-7} for $G/D = 100$). Three different gas-to-dust (G/D) ratios of 100 (red), 1000 (green), and 10000 (blue) are shown. The fluxes observed by Salyk et al. (2009) ($14 \mu\text{m}$) and Mandell et al. (2012) ($3 \mu\text{m}$) are given in black dashed lines.

tween LTE and non-LTE models can differ considerably, since IR pumping can efficiently pump molecules out to several au. This indicates that if very small emitting regions are found from observations, they may be attributed to changes in the chemistry rather than excitation effects.

Infrared pumping results in a narrow and “peaky” line profile, e.g. of the $3 \mu\text{m}$ $10^0 - 0000$ R(6) line, which are somewhat similar to the line profiles found by Bast et al. (2011) in velocity resolved observations of CO ro-vibrational lines. The CO line profiles do not have a central dip as HCN, maybe due to line opacity effects (Figure 7 in Elitzur et al. 2012) or the spectral resolution. For CO, spectro-astrometry constrains the emitting region to be smaller than a few au and a disk wind has thus been employed to explain the line profile (Pontoppidan et al. 2011). Since the HCN lines observed by CRIFES are much weaker than the CO lines, spectro-astrometry cannot be used for HCN and the line profiles are too noisy for a direct comparison. Since it is unclear, if HCN follows CO, we cannot currently distin-

guish between a disk wind scenario and extended emission due to IR pumping for HCN. Our HCN results however show that IR pumping can also result in peaky profiles.

Both models with constant HCN abundance or jump abundance with an elevated inner and lowered outer abundance can simultaneously reproduce the $3 \mu\text{m}$ and $14 \mu\text{m}$ observations reasonably well. The jump abundance models however yield much broader line profiles both at $3 \mu\text{m}$ and $14 \mu\text{m}$. Comparing non-LTE with LTE models, only an increase in line width of the $3 \mu\text{m}$ line was found. Thus, to observationally distinguish between excitation and abundance structure effects based only on line profiles, both emission bands need to be velocity resolved. Constraining the position of the abundance jump (T_{jump}) will help to test if the size of the emitting region of water and HCN is similar. Different assumptions about the size of the HCN region can lead to more than an order of magnitude different column densities and thus HCN/ H_2O abundance ratios (e.g., Salyk et al. 2011, Carr & Najita 2011). If the size of the HCN emitting region proves to be similar to that of H_2O for sources where the line profiles can be spectrally resolved, this would greatly facilitate future analyses of large samples of sources with spectrally unresolved data, such as observed with Spitzer and expected with MIRI.

Since collisional excitation is not important for most models, the gas-to-dust ratio and HCN fractional abundance are degenerate and only the absolute amount and not the fractional abundances of HCN can be determined. While this degeneracy does not alter the ratio between the $3 \mu\text{m}$ and $14 \mu\text{m}$ lines, changes in the dust opacity (e.g., through grain growth) can also change the line ratio. The degeneracy between gas-to-dust ratio and HCN fractional abundance is broken for models where most of the emission is from the innermost 2 au because of the adopted abundance profile. Then, collisional excitation can be important for the $14 \mu\text{m}$ line. For AS 205 (N), this yields a constraint for the gas-to-dust ratio > 100 . This constraint is thus explained by a different effect than that found by Meijerink et al. (2009) for water. For water, the fractional abundance is fixed as all oxygen is driven into water in hot gas ($T > 250$ K), and the gas-to-dust ratio needs to be increased until a large enough water column density is above the $\tau_{\text{dust}} = 1$ surface to yield the observed line-to-continuum ratio. In contrast to water, the HCN abundance is not fixed by an elemental abundance and is a *free parameter*. Thus, the observed line-to-continuum ratio of HCN can be reproduced by adjusting the fractional abundance and does not drive to the conclusion of a high gas-to-dust ratio as in water found by Meijerink et al. (2009).

The ro-vibrational lines of HCN show considerably different excitation effects than water (Meijerink et al. 2009). Radiative pumping is far more important for HCN, since the upper levels of the observable lines can be directly radiatively pumped from the vibrational ground-state in which most molecules are throughout the disk. In water, however, mostly pure rotational lines are observed and selection rules force radiative pumping through steps up the ladder and collisional pumping will be more important. Thus, the excitation of the vibrational lines of acetylene (C_2H_2) near $14 \mu\text{m}$ is likely similar to HCN. Indeed, non-LTE models of C_2H_2 by Lacy (2013) show the importance of radiative pumping. As for HCN, he finds that the level population is not too far from the LTE. It is thus unlikely that the trends found between HCN and C_2H_2 (Pascucci et al. 2009) can be entirely attributed to excitation effects. Following this comparison between HCN and C_2H_2 , the level structure of CO_2 (e.g., González-Alfonso & Cernicharo 1999, Figure 5) suggests that also its excitation is predominantly by radiation. It should be

noted, though, that this comparison of HCN with C_2H_2 and CO_2 is only valid if collisional excitation rates are similar, since collisional excitation has some importance for the $14\ \mu\text{m}$ lines of HCN in jump abundance models. The CO_2 - H_2 rate coefficient for the collisional de-excitation of the ν_2 bending mode is on the order of $6 \times 10^{-12}\ \text{cm}^3\ \text{s}^{-1}$ (see Boonman et al. 2003 and Allen et al. 1980) similar to the ν_2 bending mode of HCN- H_2 ($1.3 \times 10^{-11}\ \text{cm}^3\ \text{s}^{-1}$). Also the C_2H_2 - H_2 rate coefficient for the ν_5 bending mode is with $3 \times 10^{-12}\ \text{cm}^3\ \text{s}^{-1}$ (Hager et al. 1981) on the same order of magnitude.

4.2. Abundances and comparison to chemical models

The line fluxes are not affected in a major way by the LTE assumption and our derived fractional abundances do not substantially differ from previous estimates. For AS 205 (N), Mandell et al. (2012) derive a HCN fractional abundance of 2×10^{-7} relative to H_2 from only the $3\ \mu\text{m}$ lines. They used an LTE model with a gas-to-dust ratio of 12800 and smaller grains, similar to those discussed in Section 3.4. Our LTE model for the same abundance, gas-to-dust ratio of 12850 and small grains, yields a flux of $3.9 \times 10^{-15}\ \text{erg}\ \text{s}^{-1}\ \text{cm}^{-2}$ for the $3\ \mu\text{m}$ R(6) line, within about 20 % to the observed flux, confirming the agreement between our and their approach.

The derived fractional abundances (Table 2) are within the range predicted by chemical models (e.g., Markwick et al. 2002; Agúndez et al. 2008; Willacy & Woods 2009; Walsh et al. 2010; Najita et al. 2011; Walsh et al. 2012, 2014). As noted by Mandell et al. (2012), they predict a HCN to H_2O fractional abundances in the warm ($T \gtrsim 200\ \text{K}$) gas of $10^{-4} - 10^{-1}$, leading to HCN fractional abundances between 10^{-8} and 10^{-5} . In colder regions, the HCN abundance is predicted to be much lower (e.g., Figure 1 in Agúndez et al. 2008) and our models with jump abundance profiles indeed require $x_{\text{in}} > x_{\text{out}}$. While for AS 205 (N), it is difficult to distinguish between constant and jump abundance profiles with the current spectrally unresolved data (Section 3.6), it is interesting that other disks point to a jump abundance (Pontoppidan & Blevins 2014).

4.3. Predictions for JWST-MIRI, METIS, and ALMA

The MIRI instrument on JWST (Wright et al. 2004) will have a substantially better sensitivity and higher spectral resolution ($R = 3000$) compared to *Spitzer* ($R = 600$). This will allow us to detect resolved single lines of the $7\ \mu\text{m}$ and $14\ \mu\text{m}$ P- and R-branches. The Q-branches will however still be seen as a blend of several lines. Figure 12 shows MIRI predictions of the three models with $G/D = 1000$ and constant or jump abundance. Abundances given in Table 2 are used. The inset in the figure magnifies the Q-branches at $14\ \mu\text{m}$ and also includes $H^{13}\text{CN}$, calculated under the assumption of an abundance ratio $60 = [^{12}\text{C}]/[^{13}\text{C}]$. The line detection limit of MIRI⁶ corresponds to line peaks of a few mJy for $R = 3000$ even after a minimum exposure time of only 30 seconds and all lines that can be recognized in the figure are easily detected, provided that a high enough signal-to-noise can be reached on the continuum (Appendix C).

MIRI predictions of the three models differ in a similar way as found with the *Spitzer* spectra in Section 3.6. Since the jump abundance models emit from warmer regions, the P- and R-branches at $14\ \mu\text{m}$ emit to higher- J transitions compared to the

model with constant abundance. The 02^0_0 -levels are more populated close to the star and thus both the Q-branch at $14.3\ \mu\text{m}$ and the $7\ \mu\text{m}$ lines are stronger in the jump abundance models. Differences between the models can be seen better in rotational diagrams (Online Figure A.2). The constant abundance model exhibits a curved shape over the whole range of transitions because of different radii probed. The jump abundance models have higher abundances in the inner region and the lines thus become optically thick, seen in a strongly curved shape of the lower- J lines. The $H^{13}\text{CN}$ isotopologue is predicted to be easily detected and identified by its Q-branch at $\sim 14.05\ \mu\text{m}$, which is sufficiently shifted in wavelength not to be blended with the main isotopologue. We conclude that thanks to high sensitivity and spectral resolution of MIRI, it will be possible to distinguish between models with different abundance structures and to directly study the chemistry in regions were terrestrial planets form.

The METIS instrument on the E-ELT (Brandl et al. 2014) will be able to observe at $3\text{--}14\ \mu\text{m}$ with a spectral resolving power of $R = 10^5$ at $3\ \mu\text{m}$ and $R = 5000$ at $14\ \mu\text{m}$. In the Online Figure A.4, the line profiles of the $3\ \mu\text{m}$ R(6) and $14\ \mu\text{m}$ Q(6) lines from the same models as in Figure 12 are shown. At $14\ \mu\text{m}$, the velocity profile cannot be resolved, but single lines of the P- and R-branches can be seen, similar to MIRI. The factor of 100 better sensitivity of METIS compared to CRIRES will allow us to easily detect the $3\ \mu\text{m}$ lines of HCN velocity resolved. These velocity resolved observations with a good signal-to-noise ratio will simplify to constrain the position of the abundance jump (T_{jump}) and to better quantify the inner disk chemistry.

ALMA cannot resolve the inner few au, but several sub-millimeter lines within vibrationally excited states emerge from that region and are in the wavelength range of ALMA receivers. Compared to envelopes of protostars, where these submillimeter lines are regularly detected, the size of the emitting regions is very small in disks. We find that the most promising line for a detection is the $J = 4 - 3$ line within the 01^1_0 level (356.256 GHz). For the three models with $G/D = 1000$ and constant or jump abundance (Table 2), the total line fluxes vary between $82\ \text{mJy}\ \text{km}\ \text{s}^{-1}$ (constant), $26\ \text{mJy}\ \text{km}\ \text{s}^{-1}$ ($T_{\text{jump}} = 200\ \text{K}$) and $10\ \text{mJy}\ \text{km}\ \text{s}^{-1}$ ($T_{\text{jump}} = 300\ \text{K}$). For a one hour integration with 50 12m antennas and 2nd quantile weather, the 1σ -sensitivity of ALMA is $6\ \text{mJy}\ \text{km}\ \text{s}^{-1}$. Thus, while the constant abundance model can be detected within one hour, the jump abundance models require a longer integration time for a detection. The Online Figure A.3 shows the spectra of the three models together with the detection limit for $5\ \text{km}\ \text{s}^{-1}$ channels within 3 hours indicated. Depending on the abundance structure, ALMA may thus be able to detect lines between vibrationally excited levels and thus probe the inner few au of a protoplanetary disk.

5. Conclusions

We have modeled the non-LTE excitation of ro-vibrational lines of the organic molecule HCN, a chemically important ingredient of protoplanetary disks. Single point slab models to study the relative importance of different excitation effects were calculated and the emission of the T Tauri disk AS 205 (N) was modeled. That disk was observed in different vibrational bands by VLT-CRIRES at $3\ \mu\text{m}$ and *Spitzer* at $14\ \mu\text{m}$. Models with different abundance structures, gas-to-dust ratios and dust opacities were run to explore the effect on the ro-vibrational lines. The main conclusions of this study are:

⁶ <http://www.stsci.edu/jwst/instruments/miri/sensitivity/>, $\sim 10^{-20}\ \text{W}\ \text{m}^{-2}$ after $10^4\ \text{s}$

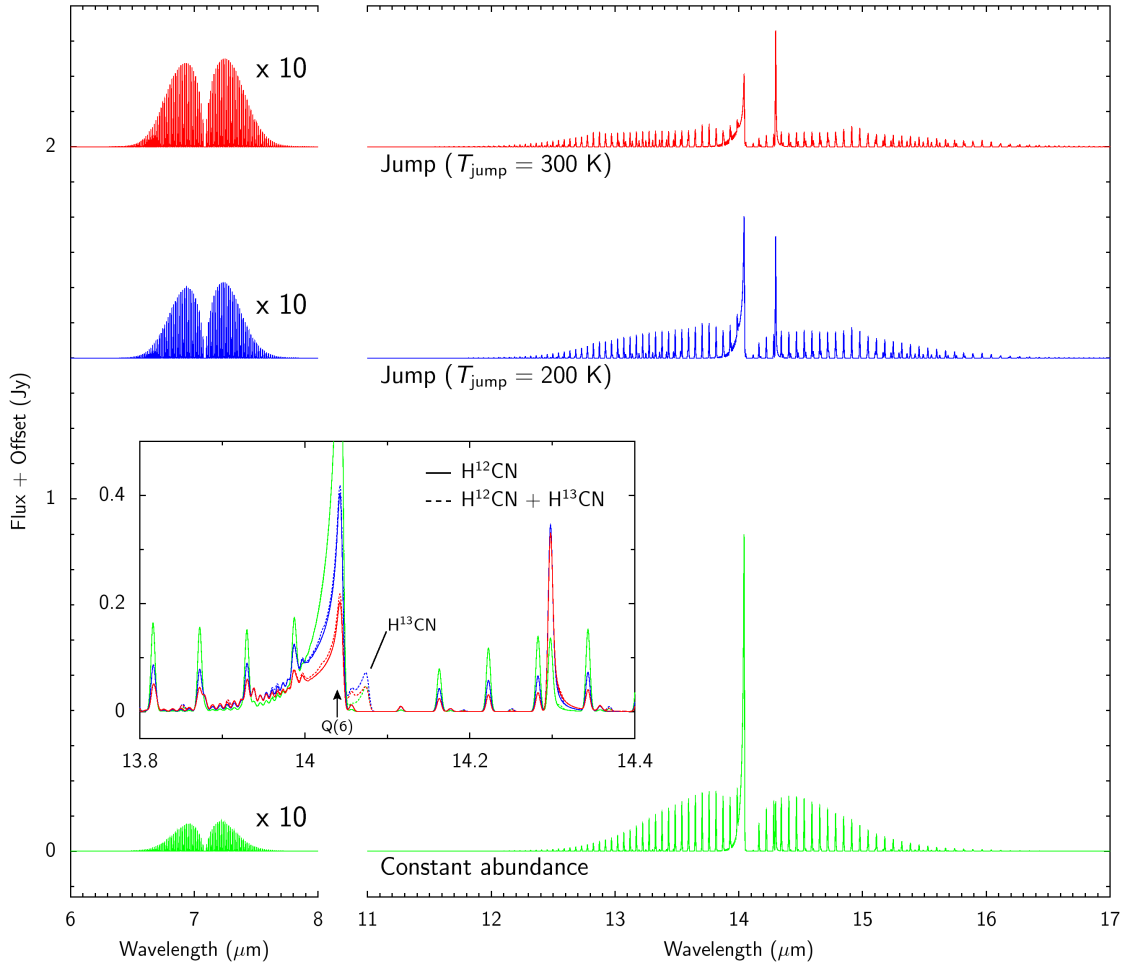


Fig. 12. Predictions for JWST-MIRI. The models given in Table 2 with $G/D=1000$ and constant or jump abundance are shown, convolved to the spectral resolving power of $R=3000$. The inset also shows a spectrum of both H^{12}CN and H^{13}CN (dashed line).

- The ro-vibrational lines of HCN have very high critical densities and collisional excitation alone can only reproduce the observed ratio between 3 and $14\ \mu\text{m}$ lines for density $> 10^{13}\ \text{cm}^{-3}$ and temperatures $> 750\ \text{K}$. Radiative pumping by IR photons can easily reproduce the observed line ratio.
- Infrared pumping can excite both the 3 and $14\ \mu\text{m}$ lines out to considerable radii of $\sim 10\ \text{au}$. It may thus point to a chemical rather than an excitation effect, if smaller emitting regions are found (e.g., by spatially or velocity resolved observations).
- Fluxes derived from LTE or non-LTE models differ not more than about a factor of ~ 3 as a result of the IR pumping of HCN. Consequently, the abundances derived by LTE and non-LTE models do not differ by a larger factor. The line profiles of the $3\ \mu\text{m}$ lines can however differ considerably.
- Both models with a constant abundance and a jump abundance, as expected from chemical considerations, can reproduce the observed fluxes reasonably well. The line profiles and extent of the emitting area however differ considerably. While it is difficult to distinguish between the scenarios with current data, it will be easily possible with JWST-MIRI and E-ELT METIS observations. Depending on the scenario, ALMA can detect rotational lines within vibrationally excited levels.
- The gas-to-dust ratio and fractional abundance of HCN are degenerate, since collisional excitation is mostly unimportant. The adopted dust opacity may change the line fluxes in

a similar way but can also alter the ratio between the 3 and $14\ \mu\text{m}$ lines.

Our work shows that despite the very high critical densities of ro-vibrational lines, the LTE assumption does not necessarily lead to large difference in the derived abundances, because of radiative pumping by the continuum radiation field. This will facilitate future studies of warm inner disk chemistry considerably, since other key molecules (C_2H_2 and CO_2) are also expected to be excited in a similar way.

Acknowledgements. We thank Jeanette Bast, Alan Heays, Fred Lahuis, Klaus Pontoppidan, Ian Smith, Xander Tielens, and an anonymous referee for useful discussions and Colette Salyk for sharing her water model of AS 205 (N). Astrochemistry in Leiden is supported by the Netherlands Research School for Astronomy (NOVA), by a Royal Netherlands Academy of Arts and Sciences (KNAW) professor prize, and by the European Union A-ERC grant 291141 CHEMPLAN.

References

- Agúndez, M., Cernicharo, J., & Goicoechea, J. R. 2008, *A&A*, 483, 831
 Allen, D., Scragg, T., & Simpson, C. 1980, *Chemical Physics*, 51, 279
 Andrews, S. M., Wilner, D. J., Hughes, A. M., Qi, C., & Dullemond, C. P. 2009, *ApJ*, 700, 1502
 Barber, R. J., Strange, J. K., Hill, C., et al. 2014, *MNRAS*, 437, 1828
 Barger, T., Wodtke, A. M., & Bowman, J. M. 2003, *ApJ*, 587, 841
 Bast, J. E. 2013, PhD thesis, Leiden Observatory
 Bast, J. E., Brown, J. M., Herczeg, G. J., van Dishoeck, E. F., & Pontoppidan, K. M. 2011, *A&A*, 527, A119

- Bast, J. E., Lahuis, F., van Dishoeck, E. F., & Tielens, A. G. G. M. 2013, *A&A*, 551, A118
- Benz, A. O., Stauber, P., Bourke, T. L., et al. 2007, *A&A*, 475, 549
- Bergin, E. A., Aikawa, Y., Blake, G. A., & van Dishoeck, E. F. 2007, *Protostars and Planets V*, B. Reipurth, D. Jewitt, and K. Keil (eds.), University of Arizona Press, Tucson, 751
- Blake, G. A. & Boogert, A. C. A. 2004, *ApJ*, 606, L73
- Boonman, A. M. S., Stark, R., van der Tak, F. F. S., et al. 2001, *ApJ*, 553, L63
- Boonman, A. M. S., van Dishoeck, E. F., Lahuis, F., et al. 2003, *A&A*, 399, 1047
- Brandl, B. R., Feldt, M., Glasse, A., et al. 2014, *ArXiv e-prints* (arXiv:1409.3087)
- Bruderer, S. 2013, *A&A*, 559, A46
- Bruderer, S., van Dishoeck, E. F., Doty, S. D., & Herczeg, G. J. 2012, *A&A*, 541, A91
- Cannon, B. & Smith, I. 1984, *Chemical Physics*, 83, 429
- Carr, J. S. & Najita, J. R. 2008, *Science*, 319, 1504
- Carr, J. S. & Najita, J. R. 2011, *ApJ*, 733, 102
- Cernicharo, J., Yamamura, I., Gonzalez-Alfonso, E., et al. 1999, *ApJ*, 526, L41
- Chandra, S. & Sharma, A. K. 2001, *A&A*, 376, 356
- Chapillon, E., Guilloteau, S., Dutrey, A., Pietu, V., & Guelin, M. 2012, *A&A*, 537, A60
- Doppmann, G. W., Najita, J. R., & Carr, J. S. 2008, *ApJ*, 685, 298
- Doty, S. D., van Dishoeck, E. F., van der Tak, F. F. S., & Boonman, A. M. S. 2002, *A&A*, 389, 446
- Draine, B. T. & Lee, H. M. 1984, *ApJ*, 285, 89
- Dumouchel, F., Faure, A., & Lique, F. 2010, *MNRAS*, 406, 2488
- Dutrey, A., Guilloteau, S., & Guelin, M. 1997, *A&A*, 317, L55
- Elitzur, M., Asensio Ramos, A., & Ceccarelli, C. 2012, *MNRAS*, 422, 1394
- Evans, N. J., Dunham, M. M., Jorgensen, J. K., et al. 2009, *ApJS*, 181, 321
- Faure, A. & Josselin, E. 2008, *A&A*, 492, 257
- Fedele, D., Bruderer, S., van Dishoeck, E. F., et al. 2013, *A&A*, 559, A77
- Gibb, E. L., Van Brunt, K. A., Brittain, S. D., & Rettig, T. W. 2007, *ApJ*, 660, 1572
- Gonzalez-Alfonso, E. & Cernicharo, J. 1999, in *ESA Special Publication*, Vol. 427, *The Universe as Seen by ISO*, ed. P. Cox & M. Kessler, 325
- Hager, J., Krieger, W., & Pfab, J. 1981, *J. Chem. Soc., Faraday Trans. 2*, 77, 469
- Harris, G. J., Larner, F. C., Tennyson, J., et al. 2008, *MNRAS*, 390, 143
- Herbst, E. & van Dishoeck, E. F. 2009, *ARA&A*, 47, 427
- Kastner, J. H., Zuckerman, B., Weintraub, D. A., & Forveille, T. 1997, *Science*, 277, 67
- Lacy, J. H. 2013, *ApJ*, 765, 130
- Lahuis, F. & van Dishoeck, E. F. 2000, *A&A*, 355, 699
- Lahuis, F., van Dishoeck, E. F., Boogert, A. C. A., et al. 2006, *ApJ*, 636, L145
- Lee, L. C. 1984, *ApJ*, 282, 172
- Mandell, A. M., Bast, J., van Dishoeck, E. F., et al. 2012, *ApJ*, 747, 92
- Markwick, A. J., Ilgner, M., Millar, T. J., & Henning, T. 2002, *A&A*, 385, 632
- Meeus, G., Salyk, C., Bruderer, S., et al. 2013, *A&A*, 559, A84
- Meijerink, R., Pontoppidan, K. M., Blake, G. A., Poelman, D. R., & Dullemond, C. P. 2009, *ApJ*, 704, 1471
- Meijerink, R. & Spaans, M. 2005, *A&A*, 436, 397
- Mulders, G. D., Waters, L. B. F. M., Dominik, C., et al. 2011, *A&A*, 531, A93
- Najita, J. R., Adamkovics, M., & Glassgold, A. E. 2011, *ApJ*, 743, 147
- Najita, J. R., Carr, J. S., Pontoppidan, K. M., et al. 2013, *ApJ*, 766, 134
- Oberg, K. I., Qi, C., Fogel, J. K. J., et al. 2010, *ApJ*, 720, 480
- Oberg, K. I., Qi, C., Fogel, J. K. J., et al. 2011, *ApJ*, 734, 98
- Paganini, L., Villanueva, G. L., Lara, L. M., et al. 2010, *ApJ*, 715, 1258
- Pascucci, I., Apai, D., Luhman, K., et al. 2009, *ApJ*, 696, 143
- Pascucci, I., Herczeg, G., Carr, J. S., & Bruderer, S. 2013, *ApJ*, 779, 178
- Pontoppidan, K. M., Blake, G. A., & Smette, A. 2011, *ApJ*, 733, 84
- Pontoppidan, K. M. & Blevins, S. M. 2014, *ArXiv e-prints* (arXiv:1406.1457)
- Pontoppidan, K. M., Salyk, C., Bergin, E. A., et al. 2014, *ArXiv e-prints* (arXiv:1401.2423)
- Pontoppidan, K. M., Salyk, C., Blake, G. A., et al. 2010, *ApJ*, 720, 887
- Procaccia, I. & Levine, R. D. 1975, *J. Chem. Phys.*, 63, 4261
- Salyk, C., Blake, G. A., Boogert, A. C. A., & Brown, J. M. 2009, *ApJ*, 699, 330
- Salyk, C., Pontoppidan, K. M., Blake, G. A., et al. 2008, *ApJ*, 676, L49
- Salyk, C., Pontoppidan, K. M., Blake, G. A., Najita, J. R., & Carr, J. S. 2011, *ApJ*, 731, 130
- Schilke, P., Mehringer, D. M., & Menten, K. M. 2000, *ApJ*, 528, L37
- Schoier, F. L., van der Tak, F. F. S., van Dishoeck, E. F., & Black, J. H. 2005, *A&A*, 432, 369
- Smith, I. W. M. & Warr, J. F. 1991, *J. Chem. Soc., Faraday Trans.*, 87, 807
- Sobolev, V. V. 1960, *Moving envelopes of stars* (Harvard University Press)
- Thi, W. F., Kamp, I., Woitke, P., et al. 2013, *A&A*, 551, A49
- Thi, W.-F., van Zadelhoff, G.-J., & van Dishoeck, E. F. 2004, *A&A*, 425, 955
- Thorwirth, S., Wyrowski, F., Schilke, P., et al. 2003, *ApJ*, 586, 338
- Tielens, A. G. G. M. 2005, *The Physics and Chemistry of the Interstellar Medium* (Cambridge University Press)
- van der Tak, F. F. S., Black, J. H., Schoier, F. L., Jansen, D. J., & van Dishoeck, E. F. 2007, *A&A*, 468, 627
- van Zadelhoff, G., van Dishoeck, E. F., Thi, W., & Blake, G. A. 2001, *A&A*, 377, 566
- Veach, T. J., Groppi, C. E., & Hedden, A. 2013, *ApJ*, 765, L34
- Walsh, C., Millar, T. J., & Nomura, H. 2010, *ApJ*, 722, 1607
- Walsh, C., Millar, T. J., Nomura, H., et al. 2014, *A&A*, 563, A33
- Walsh, C., Nomura, H., Millar, T. J., & Aikawa, Y. 2012, *ApJ*, 747, 114
- Weingartner, J. C. & Draine, B. T. 2001, *ApJ*, 548, 296
- Willacy, K. & Woods, P. M. 2009, *ApJ*, 703, 479
- Wright, G. S., Rieke, G. H., Colina, L., et al. 2004, in *Society of Photo-Optical Instrumentation Engineers (SPIE) Conference Series*, Vol. 5487, *Optical, Infrared, and Millimeter Space Telescopes*, ed. J. C. Mather, 653–663

Appendix A: Online figures

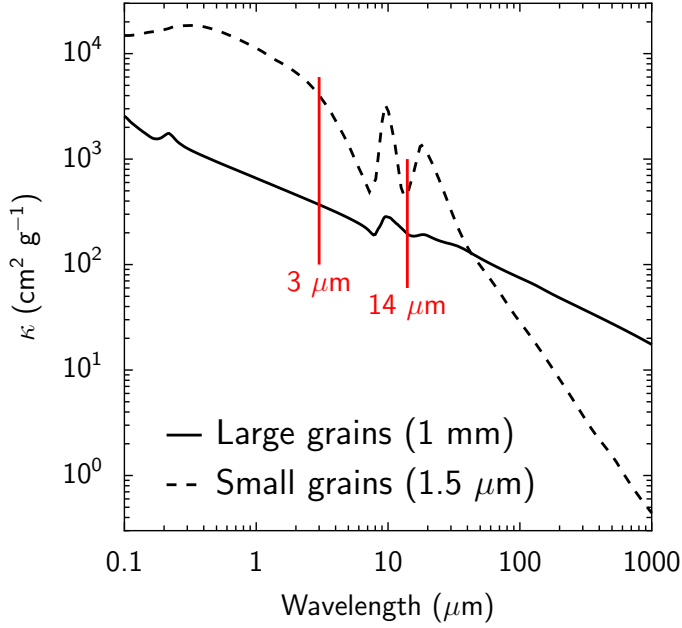


Fig. A.1. Adopted mass opacities for large vs. small ISM grains. The extinction opacity (absorption+scattering) is shown.

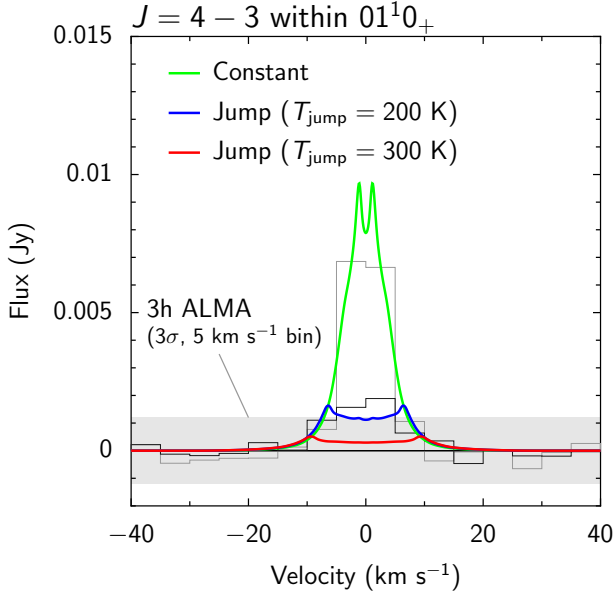


Fig. A.3. Predictions for ALMA. The $J = 4 - 3$ line within the 01^10_+ band is shown for the models given in Table 2 with $G/D = 1000$ and constant or jump abundance. The ALMA 3σ detection limit (5 km s^{-1} bin) within 3 hours is shown by the gray region. Gray lines represent the constant abundance and jump ($T_{\text{jump}} = 200 \text{ K}$) model with noise added.

Appendix B: HCN ro-vibrational collision rates

The vibrational $\text{H}_2\text{-HCN}$ collisional de-excitation rate coefficients at room temperature (297 K) of three transitions have been

measured by Smith & Warr (1991). They find for the *total* vibrational de-excitation rate coefficients between an excited state and the ground state⁷

$$\begin{aligned} k(\nu_1\nu_2\nu_3 = 100 \rightarrow 000) &= 4.70 \times 10^{-14} \text{ cm}^3\text{s}^{-1} \\ k(110 \rightarrow 000) &= 1.28 \times 10^{-11} \text{ cm}^3\text{s}^{-1} \\ k(101 \rightarrow 000) &= 1.94 \times 10^{-13} \text{ cm}^3\text{s}^{-1} \end{aligned}$$

Thus, the excitation of the stretching modes is much slower than the bending mode. Hence, we will assume that

$$\begin{aligned} k(010 \rightarrow 000) &= k(110 \rightarrow 000) \\ k(001 \rightarrow 000) &= k(101 \rightarrow 000) \end{aligned}$$

The temperature dependence of the rate coefficients is not known, but comparison with a triatomic system with similar vibrational energy and reduced mass ($\text{CO}_2\text{-H}_2$, Boonman et al. 2003 or $\text{H}_2\text{O-H}_2$, Faure & Josselin 2008) suggest, that the rate coefficients do not change by more than a factor of a few from 300 to 1000 K. This may be different for low temperatures $T \ll 300 \text{ K}$, but such cold regions do not affect the results presented in this work.

Even though strictly applicable only for stretching modes of diatomic molecules, we will approximate the rate coefficients of other transitions which only change either $\nu_i = \nu_1, \nu_2$ or ν_3 using the Landau-Teller relationship for transitions between neighboring states (Procaccia & Levine 1975 and Eqs. 6 and 8 in Chandra & Sharma 2001),

$$k(\nu_i = 2 \rightarrow 1) = k(\nu_i = 1 \rightarrow 0) \times 2 \quad (\text{B.1})$$

$$k(\nu_i = 2 \rightarrow 0) = k(\nu_i = 1 \rightarrow 0) \times 2/3 \quad (\text{B.2})$$

$$k(\nu_i = 0 \rightarrow 1) = k(\nu_i = 1 \rightarrow 0) \times \exp(-hc\omega_i/kT) \quad (\text{B.3})$$

$$k(\nu_i = 1 \rightarrow 2) = k(\nu_i = 1 \rightarrow 0) \times 2 \exp(-hc\omega_i/kT) \quad (\text{B.4})$$

$$k(\nu_i = 0 \rightarrow 2) = k(\nu_i = 1 \rightarrow 0) \times 5/3 \times \exp(-hc\omega_i/kT) \quad (\text{B.5})$$

Here, ω_i is the vibrational constant (cm^{-1}). In case a transition changes combinations of ν_1, ν_2 , and ν_3 , it is assumed that the rate coefficient is the maximum of the above rate coefficient changing one mode at the time.

Table B.1 shows the vibrational de-excitation rate coefficients calculated in this way for a temperature of 300 and 500 K.

To obtain a full set of ro-vibrational collisional rate coefficients, we employ the method suggested by Faure & Josselin (2008): Assuming a decoupling of the rotational and vibrational levels, we can write

$$k(\nu, J \rightarrow \nu', J'; T) = P_{\nu, \nu'}(T) \times k(0, J \rightarrow 0, J'; T) \quad (\text{B.6})$$

where

$$P_{\nu, \nu'}(T) = \frac{k(\nu \rightarrow \nu') \sum_J g_J \exp(-E_{\nu, J}/kT)}{\sum_J g_J \exp(-E_{\nu, J}/kT) \sum_{J'} k(0, J \rightarrow 0, J'; T)}, \quad (\text{B.7})$$

with the statistical weights g_i of the levels. This procedure ensures that the detailed balance is fulfilled. As Faure & Josselin (2008) we assume that pure rotational rate coefficients within one vibrational level are equal to the ground state rate coefficients.

The rate coefficients for the pure rotational transitions $k(0, J \rightarrow 0, J'; T)$ are taken from Dumouchel et al. (2010). The He-HCN have been scaled by the reduced weight of the $\text{H}_2\text{-HCN}$

⁷ Note that their level designation has reversed ν_1 and ν_3 with respect to ours, see Cannon & Smith (1984). In this section we use the same designation as in the remainder of our work.

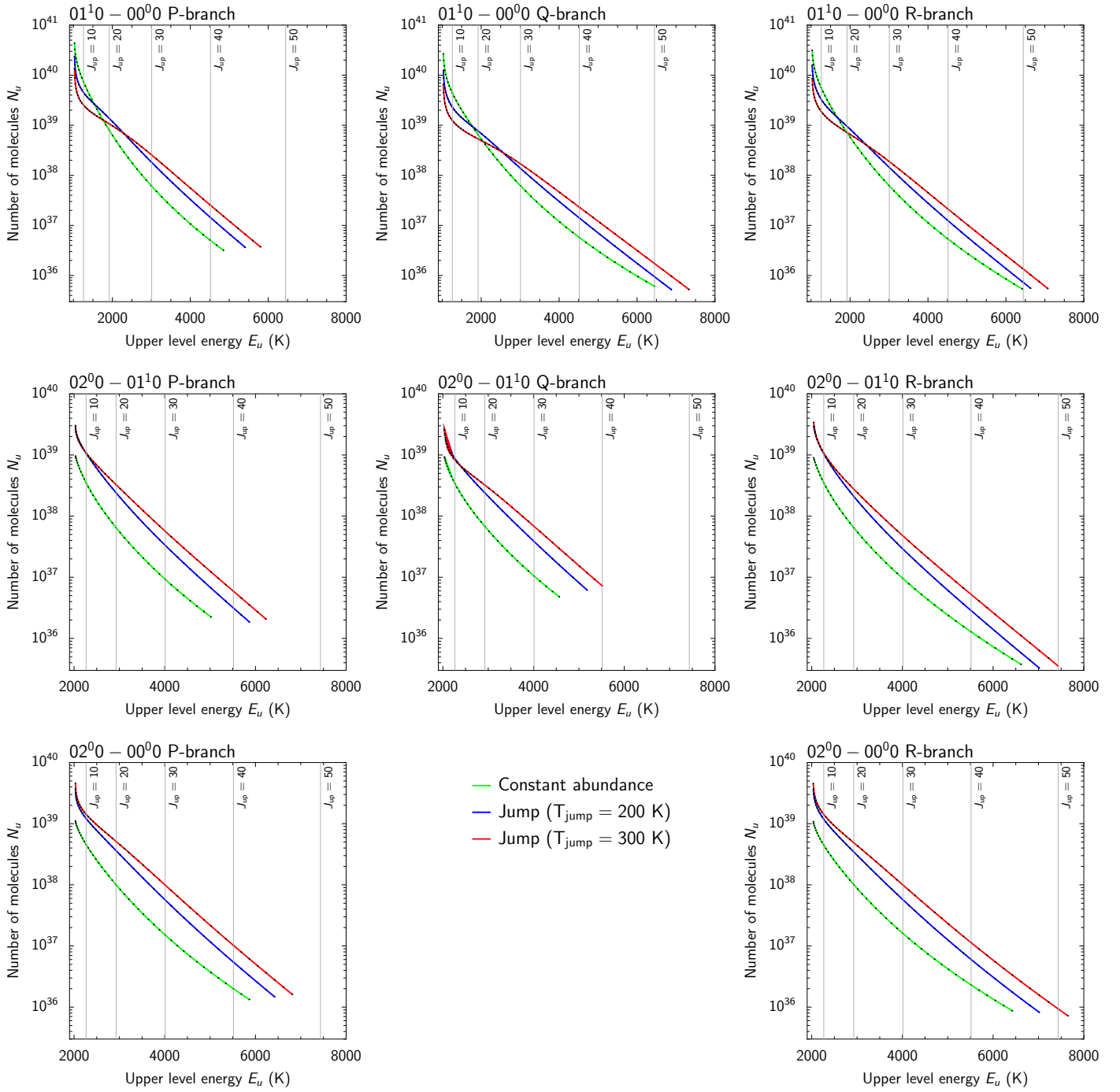


Fig. A.2. Rotational diagrams of the models given in Table 2 with $G/D=1000$ and constant or jump abundance. Only lines above the detection limit of MIRI within 10000 seconds ($\sim 10^{-20} \text{ W m}^{-2}$) are shown. The x-axis shows the upper level energy E_u (K) and the y-axis the number of molecules, $N_u = 4\pi d^2 F / (A_{ul} h \nu_{ul} g_u)$, where d is the distance, F flux, A_{ul} Einstein-A coefficient, ν_{ul} transition frequency, and g_u the upper level degeneracy.

system and levels with $J > 26$ are extrapolated using the Infinite Order Sudden (IOS) approximation as described in Section 6 of Schöier et al. (2005). The full set of derived de-excitation rate coefficients is visualized in Figure B.1 for a temperature of 500 K.

Appendix C: Line-to-continuum ratio

The line-to-continuum ratio can be the limiting factor to detect lines. For example the CRILES detections by Mandell et al.

(2012) with line-to-continuum ratios of $\sim 1\%$ in the $3 \mu\text{m}$ lines required a signal-to-noise in the continuum of several 100. Figure C.1 illustrates the line-to-continuum ratio for the non-LTE models with a constant abundance and different gas-to-dust ratios. The peak line-to-continuum ratio for different spectral resolving power ($R = \lambda/\Delta\lambda$) is shown for the R(6) $10^00 - 00^00$ line at $3 \mu\text{m}$, the Q(6) $01^10 - 00^00$ line at $14 \mu\text{m}$, and between 13.7 to $14.1 \mu\text{m}$ (mostly Q-branch of the $01^10 - 00^00$ band). The required signal-to-noise ratio in the continuum to detect a line at a 5σ level is shown in the figure.

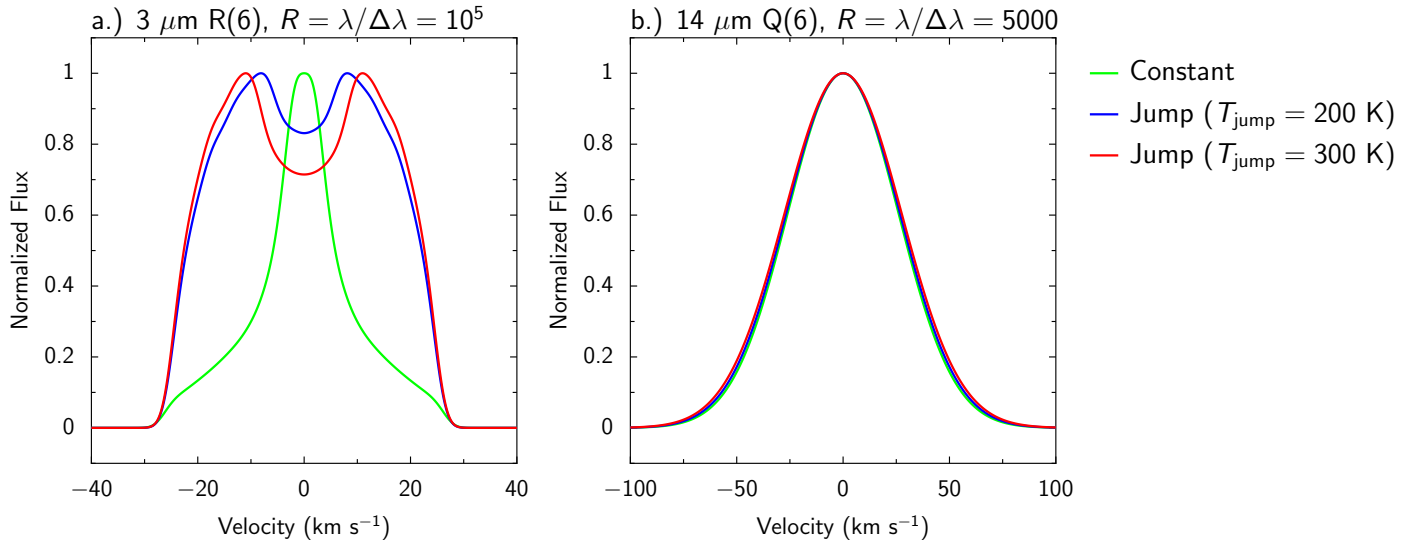


Fig. A.4. Spectrum of the **a)** R(6) $10^0_0-00^0_0$ line at $3 \mu\text{m}$ and **b)** Q(6) $01^1_0-00^0_0$ line at $14 \mu\text{m}$ of the AS 205 (N) model convolved to the spectral resolution of E-ELT METIS. The models given in Table 2 with $G/D=1000$ and constant or jump abundance are shown.

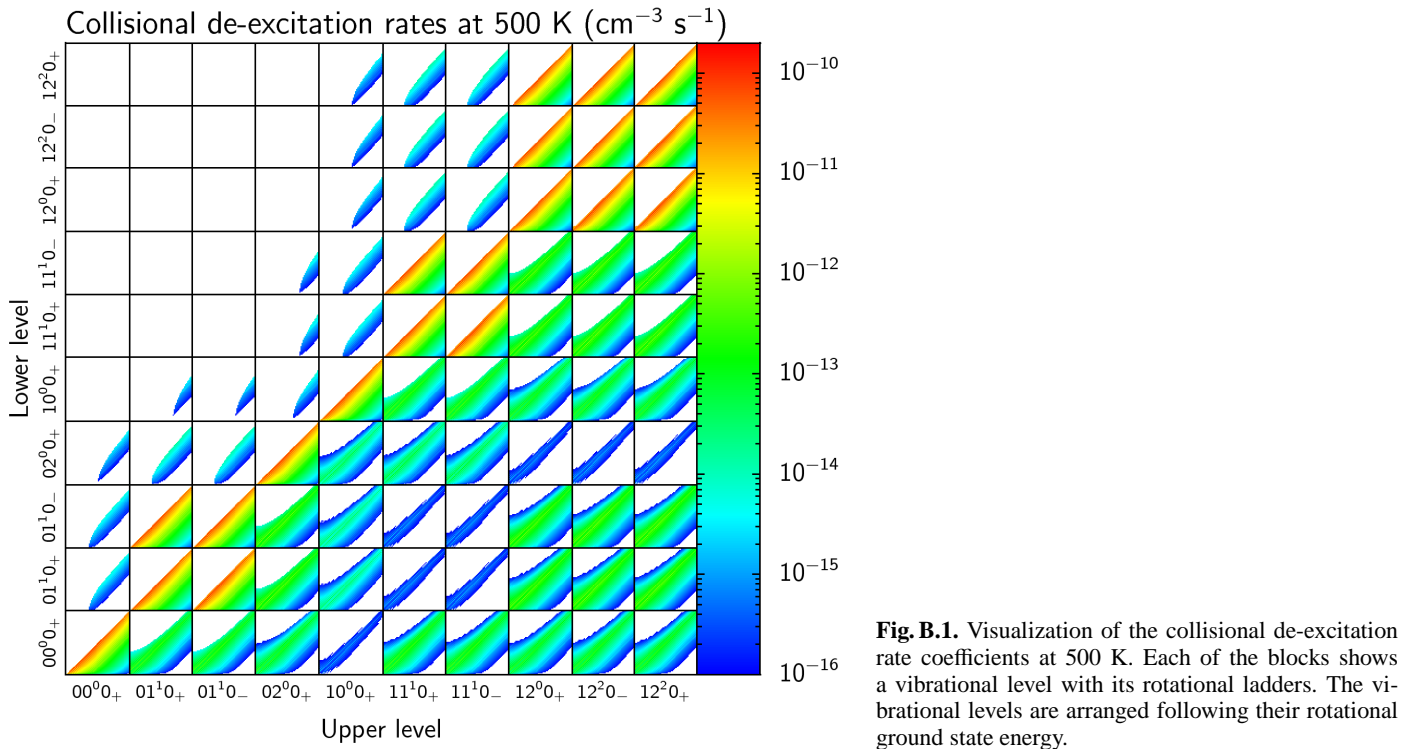


Fig. B.1. Visualization of the collisional de-excitation rate coefficients at 500 K. Each of the blocks shows a vibrational level with its rotational ladders. The vibrational levels are arranged following their rotational ground state energy.

The line-to-continuum ratio increases with the spectral resolution. The increase is strongest at low spectral resolution in the single lines. The $13.7\text{-}14.1 \mu\text{m}$ range, where several lines contribute to the peak line-to-continuum ratio, has a higher peak line-to-continuum ratio at low R . To detect the $3 \mu\text{m}$ lines, high resolution spectroscopy ($R = 10^5$) should be used, since these lines have lower line-to-continuum ratios compared to the $14 \mu\text{m}$ lines. Peak line-to-continuum ratios and line fluxes show the same degeneracy between the abundance and gas-to-dust ratio (Section 3.3). A factor of ten higher abundance, but by the same factor lower gas-to-dust ratio yields approximately the same line-to-continuum ratio. For MIRI with a spectral resolving power of $R = 3000$, a gas-to-dust ratio of 1000 and an abundance of 3×10^{-8} (Table 2), a signal-to-noise of 1000 in the continuum

will allow detecting lines down to 5 % of the peak of the Q-branch, i.e., P- and R-branch lines from high- J levels.

Table B.1. Vibrational de-excitation rate coefficients $k(v \rightarrow v')$ in $\text{cm}^3 \text{s}^{-1}$.

Initial state v	Final state v'	$k(v \rightarrow v'; 300\text{K})$	$k(v \rightarrow v'; 500\text{K})$
01 ¹ 0	00 ⁰ 0	1.28(-11)	1.28(-11)
02 ⁰ 0	00 ⁰ 0	8.53(-12)	8.53(-12)
02 ⁰ 0	01 ¹ 0	2.56(-11)	2.56(-11)
10 ⁰ 0	00 ⁰ 0	4.70(-14)	4.70(-14)
10 ⁰ 0	01 ¹ 0	3.92(-13)	1.58(-12)
10 ⁰ 0	02 ⁰ 0	6.53(-13)	2.63(-12)
11 ¹ 0	00 ⁰ 0	1.28(-11)	1.28(-11)
11 ¹ 0	01 ¹ 0	4.70(-14)	4.70(-14)
11 ¹ 0	02 ⁰ 0	7.83(-13)	3.16(-12)
11 ¹ 0	10 ⁰ 0	1.28(-11)	1.28(-11)
12 ⁰ 0	00 ⁰ 0	8.53(-12)	8.53(-12)
12 ⁰ 0	01 ¹ 0	2.56(-11)	2.56(-11)
12 ⁰ 0	02 ⁰ 0	4.70(-14)	4.70(-14)
12 ⁰ 0	10 ⁰ 0	8.53(-12)	8.53(-12)
12 ⁰ 0	11 ¹ 0	2.56(-11)	2.56(-11)

Notes. $a(b)$ means $a \times 10^b$

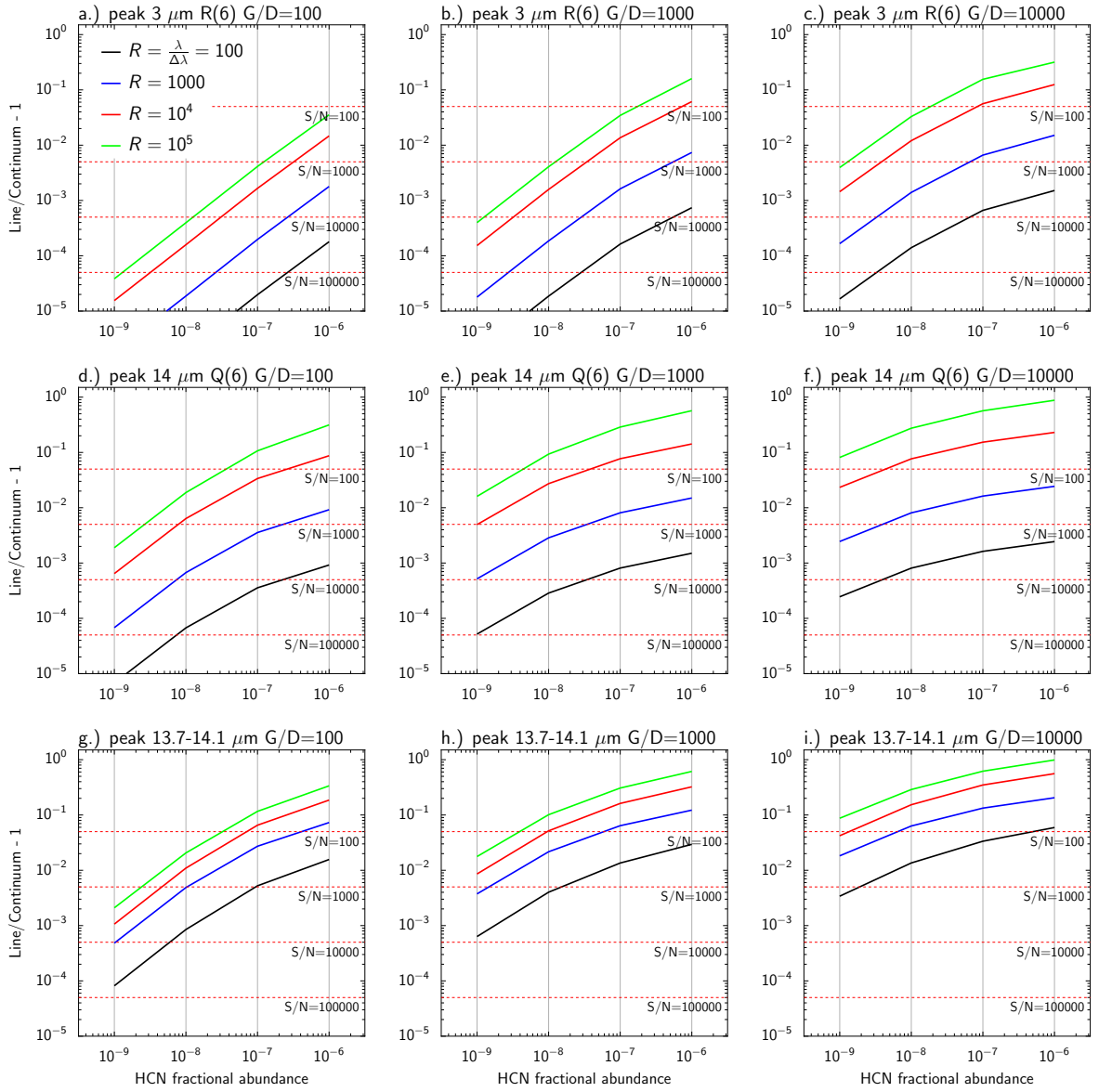


Fig. C.1. The peak line-to-continuum ratio of the **a)-c)** R(6) $10^0 - 00^0$ line at $3 \mu\text{m}$, **d)-f)** Q(6) $01^1 - 00^0$ line at $14 \mu\text{m}$, and **g)-i)** between 13.7 and $14.1 \mu\text{m}$. The non-LTE models with a constant abundance and a gas-to-dust (G/D) ratio of 100, 1000 and 100000 are shown (Figure 6), convolved to a spectral resolving power $R = \lambda/\Delta\lambda$ between 100 and 10^5 . Horizontal red dashed lines show the required signal-to-noise (S/N) in the continuum to detect a line at a 5σ level.